

Shear banding modelling in cross-anisotropic rocks

B. Pardoen^{a,1,*}, D.M. Seyedi^b, F. Collin^a

^a*ArGEnCo Department, University of Liège, Allée de la Découverte 9, 4000 Liège, Belgium*

^b*Fluid and Solid Mechanics Department, Research and Development Division, Andra, Rue Jean Monnet 1-7, 92298 Châtenay-Malabry, France*

Abstract

Sedimentary geomaterials such as rocks frequently exhibit cross-anisotropic properties and their behaviour depends on the direction of loading with respect to their microstructure. As far as material rupture is concerned, localised deformation in shear band mode appears generally before cracks and material failure. The influence of cross-anisotropy on the shear strain localisation remains an important issue and is investigated in the present study. To do so, a constitutive elastoplastic cross-anisotropic model that includes anisotropy both on the elastic and plastic characteristics is defined. For the plastic part of the model, the anisotropy of a strength parameter is introduced with a microstructure fabric tensor. Then, the fractures are modelled with finite element methods by considering the development of shear strain localisation bands and an enriched model is used to properly reproduce the shear banding. The cross-anisotropy influence on shear banding is studied through numerical applications of small and large-scale geotechnical problems that engender fractures. The two considered applications are a plane-strain biaxial compression test and an underground gallery excavation. The numerical results provide information about the influence of cross-anisotropy on the appearance and development of shear bands. It has been noticed, among other observations, that the material strength vary with the loading direction and that the development and the shape of the ex-

*Corresponding author. Tel.: +32 4366 2033.

Email address: b.pardoen@ulg.ac.be (B. Pardoen)

¹FRIA, F.R.S.-FNRS scholarship holder

cavation fractured zone that develops around a gallery is strongly influenced by the material anisotropy.

Keywords: Cross-anisotropy, shear banding, strain localisation, numerical modelling, second gradient model

1. Introduction

Geomaterials frequently feature an anisotropic behaviour related to their original fabric (Casagrande & Carillo, 1944). Among them, sedimentary materials are vertically deposited in a succession of layers and their structures
5 are composed of bedding planes. Due to this structural arrangement, the anisotropic properties of such materials often exhibit a certain type of symmetry with isotropic properties in the bedding planes. These materials are said to be transversely isotropic or cross-anisotropic (Amadei, 1983) and their behaviour and response to external solicitations depend on the loading direction
10 with respect to their microstructure.

Since the material behaviour and failure constitute crucial issues in many geotechnical problems, various theories and failure criteria have been developed (Graham & Houlsby, 1983; Duveau et al., 1998; Abelev & Lade, 2004; Lade, 2007). Concerning the material rupture, it is commonly accepted that damage
15 and localised deformation appear before the failure in many cases. Under a compressive regime when the rupture is essentially governed by shear failure, strain can accumulate in limited zones, generally in shear band mode (Desrues, 2005), and this accumulation can lead to material damage, to the development of macro-cracks (fractures) and to material rupture (Diederichs, 2003).

20 The influence of cross-anisotropy on the material behaviour and on the shear strain localisation has been investigated by different authors (Abelev & Lade, 2003; Tejchman et al., 2007; Lade et al., 2008). They concluded that the material strength as well as the shear band pattern on small-scale specimens may vary with the direction of loading or with the orientation of the bedding planes. On
25 a large scale, the material cross-anisotropy may also influence the development

of fractures around underground galleries as indicated by Armand et al. (2014) and Marschall et al. (2008).

The main objective of this study is to analyse the influence of the material cross-anisotropic features on the fracturing modelled with shear strain localisation bands. It will be investigated with finite element methods for a cross-anisotropic rock, both on a small and on a large scales. Firstly, evidences of the material anisotropy influence on the fracturing is discussed in Section 2. Secondly, the theoretical models are detailed in Section 3 where two major points are developed : a constitutive elastoplastic cross-anisotropic model and an appropriate method for the reproduction of shear banding in geomaterials. The anisotropy is taken into account in the constitutive elastoplastic model both in the elastic and plastic behaviours. For the plasticity, the anisotropy of a strength parameter (the material cohesion) is introduced with a second order microstructure fabric tensor which is a measure of the material fabric that describes the spatial distribution of the considered strength parameter (Pietruszczak & Mroz, 2000; Pietruszczak et al., 2002). The cohesion therefore specifies the effect of the loading orientation relative to the material microstructure directions. Then, an appropriate method is needed to properly model the strain localisation and shear banding with finite element methods. In fact, local descriptions of the failure are not efficient in the reproduction of strain localisation because they suffer a mesh dependency as indicated by Pietruszczak & Mróz (1981), Zervos et al. (2001b) and Collin et al. (2009b). An enhanced model introducing an internal length scale is needed and, among the existing ones, the coupled local second gradient model is used. This model includes an enrichment of the continuum with microstructure effects (Chambon et al., 2001) that comes in addition to the classical macrokinematics.

Finally, the influence of cross-anisotropy on shear strain localisation is investigated in saturated rocks with hydro-mechanical numerical applications. The modelling are performed with the non-linear finite element code Lagamine developed at the University of Liège (Charlier, 1987; Collin, 2003). A plane-strain biaxial compression test and the excavation of an underground gallery are con-

sidered among various geotechnical problems generating fractures. Concerning the biaxial compression, we investigate the appearance of shear banding and its orientation as well as the effect of bedding planes rotation. For the gallery excavation modelling, a particular attention is paid to the development of an excavation fractured zone around the gallery due to material anisotropy in case of initial isotropic stress state.

The main novelties of the present study consist, firstly, in the introduction of the material inherent anisotropy in finite element method involving coupled second gradient approach and, secondly, in the reproduction of strain localisation with rock anisotropy influence on a large scale around a gallery.

2. Fractures and anisotropy influence

Various geomaterials, like soils and rocks, are sedimentary materials that can exhibit an anisotropic behaviour and different responses depending on the loading direction. The first type of anisotropy is the inherent anisotropy that is related to the initial fabric of the particles assembly (Casagrande & Carillo, 1944; Arthur & Menzies, 1972; Ochiai & Lade, 1983). For sedimentary materials, a layered structure is observed because they were usually deposited vertically and were subjected to stress. Over time, this structure can lead to the creation of weakness planes called bedding planes due to metamorphism or diagenetic processes (Blümling et al., 2007). From a theoretical point of view, the anisotropic properties of such materials include a certain type of symmetry with a symmetry axis and isotropic properties in the (bedding) planes perpendicular to this axis (Abelev & Lade, 2004). This type of material is said to be transversely isotropic or cross-anisotropic (Amadei, 1983). A second possible type of anisotropy is an induced anisotropy that results of the loading and deformation following the material deposition (Arthur et al., 1977a; Abelev & Lade, 2004). During material loading, applied stresses may in fact engender a modification of the solid particles spatial arrangement which can lead to anisotropic material behaviour (Oda et al., 1985). Induced anisotropy was firstly observed by Casagrande &

Carillo (1944) in relation to soils shear failure and it can develop in materials having preexisting inherent anisotropic features as well as in inherent isotropic material.

Since the material behaviour and rupture are of importance regarding the
90 design of geotechnical works, it has been widely investigated in geomechanics. For instance, the concept of rupture surface is one of the oldest case of strain localisation and was already used in the design of works and structures few centuries ago (Coulomb, 1773). Nowadays, it is commonly assumed that localised deformation and damage can appear in materials prior to the rupture in a large
95 number of situations. This strain localisation is often considered as shear strain accumulation in band mode (Desrues, 2005). Starting from a homogeneous deformation state, the strain localisation consists in a brutal accumulation of strain in a limited zone that can lead to material damage. Once the damage threshold is reached, micro-cracks initiate, accumulate and propagate within the mate-
100 rial. This distributed damage can further lead to interconnected fractures by the onset of macro-cracks and provokes a sudden material rupture (Diederichs, 2003). Different modes of fractures exist. As far as geotechnical applications are concerned, they can be in tensile or opening mode, in shear mode or in mixed-mode, which is a combination of the two previous (Jenq & Shah, 1988).

105 The material anisotropy can have an effect on the shear strain localisation and on the fractures whether at small or at large scale. At small scale, plenty of laboratory tests on various geomaterials are dedicated to strain localisation (Vardoulakis et al., 1978; Han & Drescher, 1993; Finno et al., 1996, 1997; Alshibli et al., 2003) and we will principally focus on plane-strain biaxial compression. At large scale, among various geotechnical problems, the process of
110 underground drilling which generates fractures in the surrounding medium will be investigated.

2.1. Laboratory tests

The laboratory tests performed on geomaterials and dedicated to strain lo-
115 calisation are generally realised on triaxial or plane-strain biaxial compression

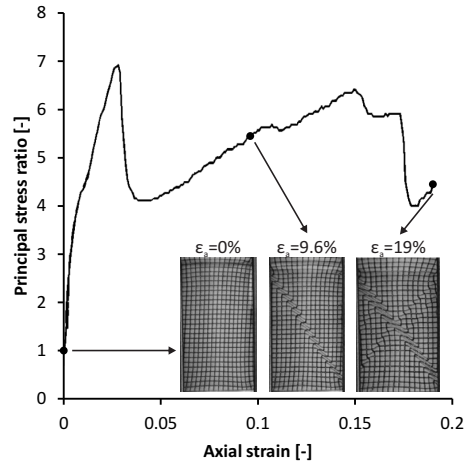


Figure 1: Shear banding formation during a plane-strain biaxial compression test on sand from Alshibli et al. (2003).

apparatus. They involve special techniques to study the evolution of the strain localisation processes (Desrues & Viggiani, 2004; Lenoir et al., 2007). The experimental results highlight that shear strain localisation is regularly observed (Fig. 1) prior to the material rupture and the establishment of a shear band
120 corresponds to a peak stress in the stress-strain global response curve of the specimen (Mokni & Desrues, 1999; Desrues, 2005). After the peak, the global reaction of the specimen generally exhibits a rapid decrease followed by whether a constant or a fluctuating reaction. This post-peak regime is dominated by the shear banding (or fracturing) process, including its structure and evolution.
125 Moreover, several shear bands (or fractures) can even initiate in a specimen after the first peak. The strain localisation as well as the post-localisation or post-peak material behaviour are therefore crucial. They need to be properly understood and represented.

The effect of cross-anisotropic fabric on the material behaviour has been investigated by different authors. Abelev & Lade (2003) and Lade et al. (2008)
130 performed different tests on sand with rotation of principal stress axes with regard to the isotropic planes of the material. They concluded that the material strength (peak value) as well as the shear band inclination and pattern may

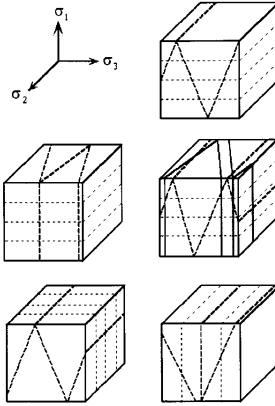


Figure 2: Shear banding patterns observed on true triaxial tests performed on Santa Monica beach sand for various material orientations from Abelev & Lade (2003).

vary with the direction of loading (Fig. 2). Among other authors, Tejchman
 135 et al. (2007) analysed the effect of fabric anisotropy on the shear strain localisation and on the stress-strain behaviour during plane-strain compression tests performed on cohesionless granular materials. They concluded that the peak stress amplitude varies with the direction of the bedding planes. However, it has only a slight influence on the shear zone thickness and inclination.

140 The previous mentioned experimental studies mostly analyse the behaviour of sand and few localisation studies are actually available on rocks (Bésuelle et al., 2000). Analysing the appearance of fractures and strain localisation in rocks is quite challenging due to their high resistance and brittle behaviour, thence the development of appropriate apparatus allowing to test this type of
 145 material is necessary (Desrues & Viggiani, 2004).

2.2. Underground excavation

The process of underground excavation generates *in situ* stress modification and damage propagation in the surrounding medium. Distinct brittle failure mechanisms can occur in the rock mass around underground galleries due to
 150 damage accumulation (Diederichs (2003), Fig. 3), those are unravelling (tensile failure), spalling (low-stress environment) and macro-scale shear failure (high-

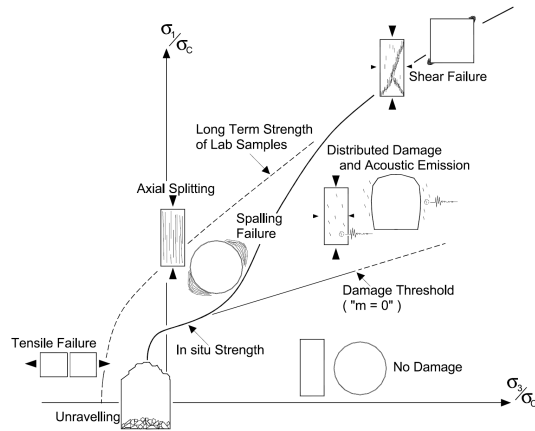


Figure 3: Rock mass brittle failure mechanisms around gallery from Diederichs (2003).

stress environment).

An excavation damaged zone therefore develops close to the drift wall with distributed damage as well as hypothetical macro-scale fractures. Inside this zone, the damage and the fracturing induce various and mainly irreversible property changes (Emsley et al., 1997; Tsang & Bernier, 2004) that engender important modifications in transport as well as in flow properties (Bossart et al., 2002; Tsang et al., 2005).

Thanks to the research on nuclear waste repository, different underground research laboratories have been developed in low permeability materials and various experimental as well as numerical studies have been conducted (Delay et al., 2007; Gens et al., 1998; Behlau & Mingerzahn, 2001; Charlier et al., 2013). Some of them permit to characterise the excavation fractured zone by means of *in situ* observations and measurements of fractures induced by deconfinement around underground galleries. Considering the Callovo-Oxfordian claystone, Armand et al. (2014) indicate that extension (spalling) and shear fractures in chevrons are detected around the galleries as well as at the excavation front face. For this material, shearing is the principal failure mechanism because of the high *in situ* stress. In the gallery axial direction, the shear chevron fractures initiate during the drilling in the rock ahead of the excavation front. In the gallery cross-

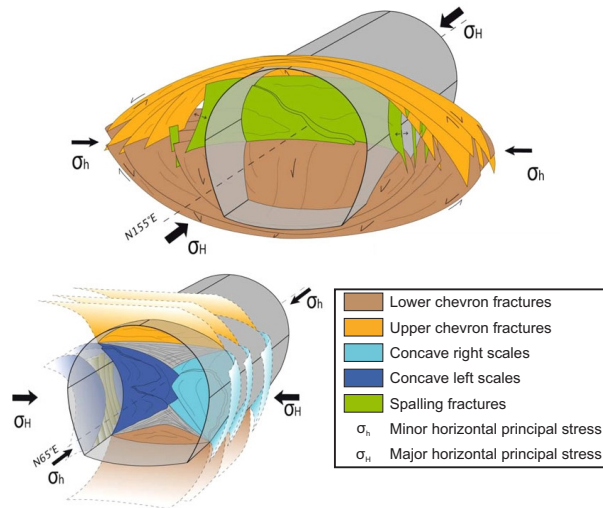


Figure 4: Conceptual model of the induced fractures in Callovo-Oxfordian claystone around a drift parallel to the major (top) and minor (bottom) horizontal principal stresses from Armand et al. (2014).

section, both types of fractures are detected close to the galleries but only shear fractures in chevrons are present deeper in the rock (Fig. 4). This chevron or herringbone fracture pattern is similar to what is observed in Boom Clay around galleries and borehole cores (Blümling et al., 2007; Wileveau & Bernier, 2008),
 175 but no extensional failure is observed in this plastic clay.

Furthermore, the excavation fractured zone in Callovo-Oxfordian claystone has an elliptical extension that can reach several meters with a significantly larger extent in one direction. The shape of the damaged zone differs for the two main drifts orientations because of the stress state anisotropy (Armand
 180 et al., 2014). In fact, for galleries oriented in the direction of the minor horizontal principal stress, the anisotropy of the stress state in the plane perpendicular to the gallery axis seems to control the fracturing patterns in the rock. Nevertheless, the development of fractures in the rock has been observed even for galleries oriented in the direction of the major horizontal principal stress (Fig. 4)
 185 that present an isotropic or quasi-isotropic stress state in their perpendicular plane (gallery section). In this case, the anisotropic extent of the fractured zone

around drifts suggests that the material anisotropy plays an important role in the onset of fractures. This role will be investigated in the present study.

Another material envisaged for nuclear waste repository is the Opalinus Clay.
190 This indurated clay features a strong material anisotropy with bedding planes inclined at about 45° with the horizontal (Martin & Lanyon, 2004). It has been observed for this material that the development of the fractures is dominated by pre-existing features (tectonic faults), extension and bedding plane instabilities (Marschall et al., 2008). The extension is the prevailing mechanism of failure
195 resulting from high differential stress and from a lower *in situ* stress state at laboratory level than for the Callovo-Oxfordian claystone. Moreover, the material anisotropy is a crucial factor in the determination of the excavation damaged zone geometry in Opalinus Clay because instabilities, such as bedding slip or buckling, can initiate due to the material weakness along the bedding planes.

200 3. Theoretical models

The fractures can be numerically modelled by various approaches. We propose to consider shear strain localisation as a predictor of the fracturing process. The displacement field is obviously discontinuous across fractures and shear banding modelling is able to reproduce this discontinuity in the sense that strain
205 localisation induces non-uniform strain distribution. The latter means that an elastic unloading is observed outside the shear band while the material remains under plastic loading inside with a concentration of the plastic strain. It results a displacement jump between the outer material located on the two sides of a shear band even if the modelling remains continuous within the band. Conse-
210 quently, such approach is mostly efficient for the reproduction of shear fractures in materials dominated by this type of failure, which is generally the case for high *in situ* stress environment (Diederichs, 2003), and for compressive regime.

Furthermore, the observations we have just mentioned in Section 2 clearly indicate that material anisotropy may have a crucial role in the development of
215 fractures in rock.

From a theoretical perspective, two major points have to be developed : firstly, a constitutive cross-anisotropic model and secondly, an appropriate method for the reproduction of shear banding in geomaterials.

3.1. Constitutive model

Geomaterials exhibit a porous structure that, relying on a mixture theory, is commonly considered as superimposed continua (Coussy, 2004). An assembly of solid grains forms the solid skeleton and fluids can fill the porous space between these grains. Generally, two fluids are considered : a wetting and a non-wetting fluid corresponding respectively to a liquid and a gaseous phase. Only saturated condition is considered in this study, meaning that the liquid phase (water) fully occupies the pores and the gaseous phase is not taken into account. The effect of fluid pressure on the Cauchy total stress field σ_{ij} is defined assuming Biot's postulate of effective stress (Biot, 1941). This definition accounts for the relative deformability of the solid structure (grain skeleton) by introducing its compressibility through the Biot's tensor :

$$\sigma_{ij} = \sigma'_{ij} + b_{ij} p_w \quad (1)$$

220 where σ'_{ij} is the Biot's effective stress field defined under soil mechanics convention in which compressive stress is positive, b_{ij} is Biot's tensor (Eq. 14) and p_w is the pore water pressure, negative if suction. Moreover, the variation of solid density ρ_s and material (mixture) porosity Φ also depend on Biot's tensor (Coussy, 2004; Detournay & Cheng, 1993).

The elastoplastic constitutive law expressing the relationship between the strain and effective stress field increments is defined as follows :

$$\tilde{\sigma}'_{ij} = C_{ijkl} \dot{\epsilon}_{kl} \quad (2)$$

where $\dot{\epsilon}_{ij} = \frac{L_{ij} + L_{ji}}{2}$ is the Cauchy strain rate corresponding to the symmetric part of the velocity gradient field $L_{ij} = \frac{\partial \dot{u}_i}{\partial x_j}$, \dot{u}_i being the time derivative of the displacement field u_i , C_{ijkl} is the elastoplastic constitutive tangent tensor for small strain and rotations and $\tilde{\sigma}'_{ij}$ is the Jaumann objective effective stress rate.

An objective derivative (independent of rigid body rotation) of the stress field is introduced through the Jaumann derivative (Jaumann, 1911) :

$$\tilde{\sigma}'_{ij} = \dot{\sigma}'_{ij} - \omega_{ij} \sigma'_{ij} + \sigma'_{ij} \omega_{ij} \quad (3)$$

225 where $\dot{\sigma}'_{ij}$ is the effective stress rate and $\omega_{ij} = \frac{L_{ij} - L_{ji}}{2}$ is the spin rate tensor corresponding to the antisymmetric part of the velocity gradient field L_{ij} . In the following equations, the notation \dot{a} corresponds to the time derivative of any quantity a .

In the context of elastoplasticity, the total strain rate $\dot{\epsilon}_{ij}$ includes an elastic $\dot{\epsilon}_{ij}^e$ and a plastic $\dot{\epsilon}_{ij}^p$ components :

$$\dot{\epsilon}_{ij} = \dot{\epsilon}_{ij}^e + \dot{\epsilon}_{ij}^p \quad (4)$$

230 The elastic and plastic theories are defined hereafter for anisotropic materials, which means that the elastoplastic properties depend on the coordinate axes to which the properties are referred and therefore depend on the orientation.

3.1.1. Linear elasticity theory

By separating the elastic and plastic components of the strain tensor, a linear elastic relationship that links the elastic strain rate $\dot{\epsilon}_{ij}^e$ to the Jaumann effective stress rate $\tilde{\sigma}'_{ij}$ through the Hooke law is expressed :

$$\tilde{\sigma}'_{ij} = C_{ijkl}^e \dot{\epsilon}_{kl}^e \quad (5)$$

where C_{ijkl}^e is the Hooke anisotropic elastic tensor (Graham & Houlsby, 1983) that must be symmetric because of thermodynamic requirement (Love, 1927).

Generally, materials show limited forms of anisotropy. For instance, an orthotropic elastic material has three mutually orthogonal symmetry planes and a cross-anisotropic one exhibits parallel isotropic planes (Lekhnitskii, 1963). In case of orthotropy and cross-anisotropy, the properties are related to the orthotropic (and orthogonal) axes e_1 , e_2 and e_3 and the (e_1, e_2, e_3) space represents the orthotropic configuration as illustrated in Fig. 5 (Amadei, 1983). The

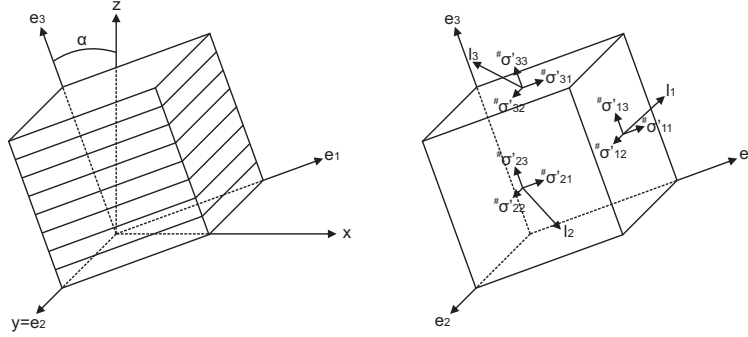


Figure 5: Principal and orthotropic axes for a representative elementary volume exhibiting cross-anisotropy : rotation of the isotropic planes (left), stress state in the orthotropic configuration and generalised loading vector (right).

Hooke's stress-strain relation is therefore formulated in the orthotropic axes as follows :

$$\# \epsilon_{ij}^e = D_{ijkl}^e \# \tilde{\sigma}_{kl} \quad (6)$$

235 where the notation $\#$ denotes a quantity in the orthotropic axes and $D_{ijkl}^e = [C_{ijkl}^e]^{-1}$ is the compliance elastic tensor obtained by inverting C_{ijkl}^e .

For cross-anisotropy, five independent parameters are needed to describe the material elasticity : E_{\parallel} , E_{\perp} , $\nu_{\parallel\parallel}$, $\nu_{\parallel\perp}$, $G_{\parallel\perp}$, where the subscripts \parallel and \perp indicate the directions parallel and perpendicular to the bedding, respectively. Considering (e_1, e_2) as the isotropic planes orientation (bedding planes for sedimentary materials) and e_3 as the normal to these planes lead to the following

definition of the elastic tensor :

$$D_{ijkl}^e = \begin{bmatrix} \frac{1}{E_{\parallel}} & -\frac{\nu_{\parallel\parallel}}{E_{\parallel}} & -\frac{\nu_{\perp\parallel}}{E_{\perp}} & 0 & 0 & 0 \\ -\frac{\nu_{\parallel\parallel}}{E_{\parallel}} & \frac{1}{E_{\parallel}} & -\frac{\nu_{\perp\parallel}}{E_{\perp}} & 0 & 0 & 0 \\ -\frac{\nu_{\parallel\perp}}{E_{\parallel}} & -\frac{\nu_{\parallel\perp}}{E_{\parallel}} & \frac{1}{E_{\perp}} & 0 & 0 & 0 \\ 0 & 0 & 0 & \frac{1}{2G_{\parallel\parallel}} & 0 & 0 \\ 0 & 0 & 0 & 0 & \frac{1}{2G_{\parallel\perp}} & 0 \\ 0 & 0 & 0 & 0 & 0 & \frac{1}{2G_{\perp\perp}} \end{bmatrix} \quad (7)$$

The equality below must be satisfied due to the symmetry of the tensor :

$$\frac{\nu_{\perp\parallel}}{E_{\perp}} = \frac{\nu_{\parallel\perp}}{E_{\parallel}} \quad (8)$$

The shear modulus in the isotropic planes is obtained as follows :

$$G_{\parallel\parallel} = \frac{E_{\parallel}}{2(1 + \nu_{\parallel\parallel})} \quad (9)$$

and the other shear modulus are equal because of the symmetry of the stress and strain tensors :

$$G_{\parallel\perp} = G_{\perp\parallel} \quad (10)$$

The Hooke's law being formulate in the orthotropic axes, a change of the reference system has to be computed to obtain the stress state :

$$\# \tilde{\sigma}'_{ij} = R_{ik} R_{jl} \tilde{\sigma}'_{kl} \quad (11)$$

where R_{ij} is the rotation matrix. Once the strain tensor rate is calculated in the orthotropic axes (Eq. 6) it can be reformulated in the global axes (x, y, z) by inverting the rotation :

$$\dot{\epsilon}_{ij}^e = R_{ki} R_{lj} \# \dot{\epsilon}_{kl}^e \quad (12)$$

The matrix of rotation is characterised by the three Euler's angles corresponding to rotations around the three orthotropic axes. In this study, only a rotation α

around e_2 is considered (Fig. 5) and gives :

$$R_{ij} = \begin{bmatrix} \cos\alpha & 0 & \sin\alpha \\ 0 & 1 & 0 \\ -\sin\alpha & 0 & \cos\alpha \end{bmatrix} \quad (13)$$

Another important aspect of the anisotropic elasticity is the compressibility of the solid grains skeleton. It is expressed through Biot's symmetric tensor which is defined for anisotropic material as follows (Cheng, 1997) :

$$b_{ij} = \delta_{ij} - \frac{C_{ijkk}^e}{3 K_s} \quad (14)$$

where δ_{ij} is the Kronecker symbol and K_s is the bulk modulus of the solid phase. The generalised Biot's coefficient reads :

$$b = \frac{b_{ii}}{3} = 1 - \frac{K}{K_s} \quad (15)$$

where K is the generalised drained bulk modulus of the poroelastic material :

$$K = \frac{C_{iijj}^e}{9} \quad (16)$$

For orthotropic and cross-anisotropic materials, the definition of Eq. 14 is valid in the orthotropic axes and reduces to a diagonal matrix. For cross-anisotropic material with isotropic planes oriented parallel to (e_1, e_2) it is expressed as follows :

$${}^{\#}b_{ij} = \begin{bmatrix} b_{\parallel} & 0 & 0 \\ 0 & b_{\parallel} & 0 \\ 0 & 0 & b_{\perp} \end{bmatrix} \quad (17)$$

with identical values in the isotropic planes. It becomes in the global axes :

$$b_{ij} = R_{ki} R_{lj} {}^{\#}b_{kl} \quad (18)$$

Adopting the micro-homogeneity and micro-isotropy assumptions (Cheng, 1997), for which the bulk modulus of the solid phase K_s is isotropic, the Biot's coefficients can be expressed as :

$$b_{\parallel} = 1 - \frac{2 C_{\parallel\parallel\parallel\parallel}^e + C_{\parallel\parallel\perp\perp}^e}{3 K_s} = 1 - \frac{1 + \nu_{\parallel\parallel} + \nu_{\parallel\parallel} \nu_{\perp\parallel} + \nu_{\perp\parallel}}{3 E_{\parallel} E_{\perp} \Upsilon K_s} \quad (19)$$

$$b_{\perp} = 1 - \frac{2 C_{\perp\perp\parallel\parallel}^e + C_{\perp\perp\perp\perp}^e}{3 K_s} = 1 - \frac{1 - \nu_{\parallel\parallel}^2 + 2 \nu_{\parallel\perp} + 2 \nu_{\parallel\perp} \nu_{\parallel\parallel}}{3 E_{\parallel} E_{\parallel} \Upsilon K_s} \quad (20)$$

$$\Upsilon = \frac{1 - \nu_{\parallel\parallel}^2 - 2 \nu_{\perp\parallel} \nu_{\parallel\perp} (1 + \nu_{\parallel\parallel})}{E_{\parallel} E_{\parallel} E_{\perp}} \quad (21)$$

For isotropic material, Biot's coefficients reduce to $b_{ij} = b \delta_{ij}$ with $b = 1 - \frac{K}{K_s}$ and $K = \frac{E}{3(1-2\nu)}$.

3.1.2. Plasticity theory

A non-associated elastoplastic internal friction model with a Van Eekelen yield surface (Fig. 6) is used for the considered material (VanEekelen, 1980). This model is broadly used in geomechanics for frictional material and includes a dependence on the third stress invariant. Van Eekelen criterion is built from the Drucker-Prager criterion by introducing a dependence on the Lode angle with the purpose of matching more closely the Mohr Coulomb criterion. This criterion incorporates a distinction between the compression and the extension friction angles. This distinction avoids an overestimation of the material extension resistance in case of high value of the compression friction angle (Barnichon, 1998). The yield surface definition, under soil mechanics convention with positive compressive stress, is :

$$F \equiv II_{\hat{\sigma}} - m \left(I_{\sigma'} + \frac{3 c}{\tan \varphi_c} \right) = 0 \quad (22)$$

where $I_{\sigma'}$ is the first stress invariant, $II_{\hat{\sigma}}$ is the second deviatoric stress invariant, m is a parameter of the yield surface, c is the cohesion and φ_c is the compression friction angle. The first and second stress invariants are defined as follows :

$$I_{\sigma'} = \sigma'_{ij} \delta_{ij} = \sigma'_{ii} \quad (23)$$

$$II_{\hat{\sigma}} = \sqrt{\frac{1}{2} \hat{\sigma}_{ij} \hat{\sigma}_{ij}} \quad (24)$$

where $\hat{\sigma}_{ij}$ is the deviatoric stress tensor given by :

$$\hat{\sigma}_{ij} = \sigma_{ij} - \frac{\sigma_{kk}}{3} \delta_{ij} \quad (25)$$

The definition of the parameter m is :

$$m = d_1 (1 + d_2 \sin(3\beta))^\eta \quad (26)$$

it depends on the Lode angle given by :

$$\sin(3\beta) = -\frac{3\sqrt{3}}{2} \frac{III_{\hat{\sigma}}}{II_{\hat{\sigma}}^3} \quad (27)$$

where $III_{\hat{\sigma}}$ is the third deviatoric stress invariant :

$$III_{\hat{\sigma}} = \frac{1}{3} \hat{\sigma}_{ij} \hat{\sigma}_{jk} \hat{\sigma}_{ki} \quad (28)$$

The three parameters d_1 , d_2 and η have to verify the conditions :

$$d_1 > 0 \quad (29)$$

$$d_2 \eta > 0 \quad (30)$$

$$-1 < d_2 < 1 \quad (31)$$

The parameter η controls the yield surface convexity and is generally chosen equal to -0.229 (default value). The other coefficients d_1 and d_2 allow independent choice of the compression and extension friction angles, φ_c and φ_e :

$$d_1 = \frac{r_c}{(1 + d_2)^\eta} \quad (32)$$

$$d_2 = \frac{\left(\frac{r_c}{r_e}\right)^{\frac{1}{\eta}} - 1}{\left(\frac{r_c}{r_e}\right)^{\frac{1}{\eta}} + 1} \quad (33)$$

where the reduced radius in compression r_c and in extension r_e read :

$$r_c = \frac{2 \sin(\varphi_c)}{\sqrt{3}(3 - \sin(\varphi_c))} \quad (34)$$

$$r_e = \frac{2 \sin(\varphi_e)}{\sqrt{3}(3 + \sin(\varphi_e))} \quad (35)$$

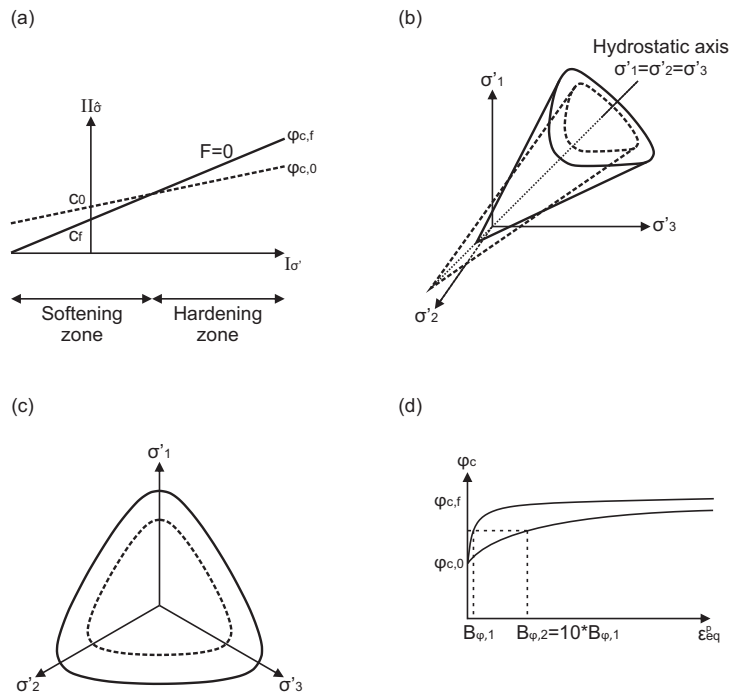


Figure 6: Van Eekelen yield surface with isotropic φ hardening and c softening : in the stress invariants plane (a), in the principal effective stress space (b), in the deviatoric plane (c) and hyperbolic evolution of φ_c hardening for two values of coefficient B_φ (d).

Cohesion and friction angles isotropic hardening and/or softening can also be considered. They evolve as a function of the Von Mises' equivalent deviatoric plastic strain $\hat{\epsilon}_{eq}^p$ which is defined as follows :

$$\hat{\epsilon}_{eq}^p = \sqrt{\frac{2}{3} \hat{\epsilon}_{ij}^p \hat{\epsilon}_{ij}^p} \quad (36)$$

where $\hat{\epsilon}_{ij}^p$ is the deviatoric plastic strain tensor calculated from the plastic strain tensor ϵ_{ij}^p :

$$\hat{\epsilon}_{ij}^p = \epsilon_{ij}^p - \frac{\epsilon_{kk}^p}{3} \delta_{ij} \quad (37)$$

The hardening/softening are introduced with hyperbolic functions (Barnichon (1998) and Fig. 6) :

$$c = c_0 + \frac{(c_f - c_0) \langle \hat{\epsilon}_{eq}^p - dec_c \rangle}{B_c + \langle \hat{\epsilon}_{eq}^p - dec_c \rangle} \quad (38)$$

$$\varphi_c = \varphi_{c,0} + \frac{(\varphi_{c,f} - \varphi_{c,0}) \langle \hat{\epsilon}_{eq}^p - dec_\varphi \rangle}{B_\varphi + \langle \hat{\epsilon}_{eq}^p - dec_\varphi \rangle} \quad (39)$$

$$\varphi_e = \varphi_{e,0} + \frac{(\varphi_{e,f} - \varphi_{e,0}) \langle \hat{\epsilon}_{eq}^p - dec_\varphi \rangle}{B_\varphi + \langle \hat{\epsilon}_{eq}^p - dec_\varphi \rangle} \quad (40)$$

240 where c_0 and c_f are the initial and final cohesions, $\varphi_{c,0}$ and $\varphi_{c,f}$ are the initial and final compression friction angles, $\varphi_{e,0}$ and $\varphi_{e,f}$ are the initial and final extension friction angles, dec_c and dec_φ are the equivalent plastic strain values from which hardening/softening starts, the coefficients B_φ and B_c are the equivalent plastic strain values for which half of the hardening/softening of friction angles and cohesion is attained, and $\langle \cdot \rangle$ are the Macaulay brackets with
245 $\langle x \rangle = x$ if $x \geq 0$ and $\langle x \rangle = 0$ if $x < 0$. The evolution of the yield surface in case of hardening of the friction angle and softening of the cohesion is detailed in Fig. 6.

For non-associated plasticity, the plastic strain rate (plastic flow) is perpendicular to a plastic potential G :

$$\dot{\epsilon}_{ij}^p = \dot{\Lambda} \frac{\partial G}{\partial \sigma'_{ij}} \quad (41)$$

where Λ is the plastic multiplier. The non-associated plastic potential is defined similarly to the plastic loading surface F :

$$G \equiv II_{\hat{\sigma}} - m_G I_{\sigma'} = 0 \quad (42)$$

where m_G is defined similarly to m in Eq. 26 but introducing dilatancy angles ψ_c and ψ_e instead of φ_c and φ_e in the reduced radius of Eq. 34 and 35 :

$$r_{c,G} = \frac{2 \sin(\psi_c)}{\sqrt{3}(3 - \sin(\psi_c))} \quad (43)$$

$$r_{e,G} = \frac{2 \sin(\psi_e)}{\sqrt{3}(3 + \sin(\psi_e))} \quad (44)$$

In addition to the anisotropic elastic behaviour detailed in the previous Section 3.1.1, the plastic behaviour and the strength parameters of the material can also be anisotropic and therefore depend on direction and orientation. Various failure criteria for anisotropic materials have been developed (Duveau et al., 1998; Lade, 2007) and hereafter, we focus on the material cohesion anisotropy which is defined with a second order microstructure fabric tensor a_{ij} describing the cohesion spatial distribution. This tensor is a measure of the material fabric and its eigenvectors correspond to the principal material microstructure axes, i.e. the orthotropic axes, e_1, e_2, e_3 . The cohesion corresponds to the projection of this tensor on a generalised unit loading vector l_i that characterises the loading direction relative to the material microstructure orientations (Pietruszczak & Mroz, 2000, 2001; Chen et al., 2010). As detailed in Fig. 5, each component of l_i corresponds to the stress resultant acting on facets of normal e_i and is defined as follows :

$$l_i = \sqrt{\frac{\# \sigma'_{i1}{}^2 + \# \sigma'_{i2}{}^2 + \# \sigma'_{i3}{}^2}{\# \sigma'_{ij} \# \sigma'_{ij}}} \quad (45)$$

where $\# \sigma'_{ij}$ is expressed in reference to the material axes. Therefore, the cohesion specifies the effect of load orientation relative to the material axes (Pietruszczak et al., 2002; Pietruszczak, 2010) :

$$c_0 = a_{ij} l_i l_j \quad (46)$$

It can also be expressed by employing the deviatoric part of the microstructure fabric tensor (Kanatani, 1984) :

$$c_0 = \bar{c}(1 + A_{ij} l_i l_j) \quad (47)$$

$$A_{ij} = \frac{\hat{a}_{ij}}{\bar{c}} = \frac{a_{ij}}{\bar{c}} - \delta_{ij} \quad (48)$$

$$\bar{c} = \frac{a_{ii}}{3} \quad (49)$$

where \bar{c} is a microstructure parameter, A_{ij} is a traceless symmetric tensor, $A_{ii} = 0$, and $\hat{a}_{ij} = a_{ij} - \frac{a_{kk}}{3} \delta_{ij}$ is the deviatoric part of the microstructure tensor a_{ij} . The above expression of Eq. 47 can be generalised by considering higher order tensors :

$$c_0 = \bar{c} \left(1 + A_{ij} l_i l_j + b_1 (A_{ij} l_i l_j)^2 + b_2 (A_{ij} l_i l_j)^3 + \dots \right) \quad (50)$$

where b_1, b_2, \dots are constants.

Considering orthotropy and referring the problem to the principal material axes imply $A_{ij} = 0$ for $i \neq j$ with $A_{ii} = A_{11} + A_{22} + A_{33} = 0$ and the projection of A_{ij} on the loading vector is :

$$A_{ij} l_i l_j = A_{11} l_1^2 + A_{22} l_2^2 + A_{33} l_3^2 \quad (51)$$

Moreover, for an isotropic stress state $l_1 = l_2 = l_3 = \sqrt{1/3}$ by Eq. 45 which leads to $A_{ij} l_i l_j = A_{ii}/3 = 0$ by Eq. 51 and to $c_0 = \bar{c}$ by Eq. 50. Therefore, \bar{c} is the cohesion of the orthotropic material subjected to an isotropic loading. Considering cross-anisotropy implies $A_{11} = A_{22} = A_{\parallel}$ and $A_{33} = -2A_{11} = -2A_{\parallel}$ if the isotropic planes are parallel to (e_1, e_2) . Thus :

$$A_{ij} l_i l_j = A_{\parallel} (1 - 3 l_3^2) \quad (52)$$

where A_{\parallel} is the component of the microstructure operator A_{ij} in the isotropic planes. The late expression for cohesion of Eq. 50 becomes :

$$c_0 = \bar{c} \left(1 + A_{\parallel} (1 - 3 l_3^2) + b_1 A_{\parallel}^2 (1 - 3 l_3^2)^2 + b_2 A_{\parallel}^3 (1 - 3 l_3^2)^3 + \dots \right) \quad (53)$$

250 The constants \bar{c} , $A_{||}$, b_1 , b_2 , ... can be obtained from experimental data and laboratory tests.

Because c_0 evolves due to the material fabric and to the loading, it is more appropriate for the cohesion softening (Eq. 38) to define a final cohesion that evolves in the same manner by $c_f = \xi c_0$, ξ being the ratio of cohesion softening.

255 3.2. Coupled local second gradient model

The appearance of strain localisation in shear band mode can be numerically modelled with finite element methods. Nevertheless, classical finite element methods fail to properly model the post-peak or post-localisation behaviour in the sense that the strain localisation suffers a mesh dependency (Pietruszczak & Mróz, 1981; Zervos et al., 2001b; Collin et al., 2009b; Wu & Wang, 2010). 260 The introduction of an internal length scale is thus crucial and can be done by considering enhanced models and regularisation methods. Two principal categories exist : one consists in the enrichment of the constitutive law with for instance non-local approaches (Bazant et al., 1984; Pijaudier-Cabot & Bazant, 1987; Peerlings et al., 1996b; Guy et al., 2012) or gradient plasticity (Aifantis, 1984; de Borst & Mühlhaus, 1992; Peerlings et al., 1996a), the other one consists in the enrichment of the continuum kinematics with microstructure effects. For this second category the microkinematics are characterised at microscale in addition to the classical macrokinematics (Cosserat & Cosserat, 1909; Toupin, 1962; 270 Mindlin, 1964; Germain, 1973). The more ancient and famous microstructure enhanced model is developed by the Cosserat brothers (Cosserat & Cosserat, 1909) who introduced local rotation degrees of freedom in addition to the displacements of classical continua. Papanastasiou & Vardoulakis (1992) were the first to present a numerical analysis of progressive localisation around excavated 275 cavity in rock with Cosserat microstructure.

The local second gradient model (Chambon et al., 1998, 2001) is chosen among the existing regularisation methods with kinematic enrichment and is used to model strain localisation. Additionally to the macroscale displacement field u_i , the strain and rotation at microscale are characterised by a microkine-

matic second order gradient field v_{ij} . The balance equations of the hydro-mechanical problem under saturated conditions (Collin et al., 2006) are written in a weak form for one of the phases and for the mixture in updated Lagrangian configuration which corresponds to the current porous material configuration Ω^t (unit volume). The notation a^t corresponds to the current configuration of any quantity a at a given time t . Based on the virtual work principle and for every kinematically admissible virtual displacement field u_i^* , the momentum balance equation of the mixture is derived from the equality between internal and external virtual works. It is expressed as follows :

$$\int_{\Omega^t} \left(\sigma_{ij}^t \frac{\partial u_i^*}{\partial x_j^t} + \tau_{ij}^t (v_{ij}^* - F_{ij}^*) + \Sigma_{ijk}^t h_{ijk}^* \right) d\Omega^t = \int_{\Gamma_\sigma^t} (\bar{t}_i u_i^* + \bar{T}_i Du_i^*) d\Gamma^t \quad (54)$$

where x_i is the current coordinate, the general notation a^* corresponds to the virtual quantity a , v_{ij}^* is the virtual microkinematic gradient, $h_{ijk}^* = \frac{\partial v_{ij}^*}{\partial x_k^t}$ is the virtual micro second gradient, $F_{ij}^* = \frac{\partial u_i^*}{\partial x_j^t}$ is the virtual macrodeformation gradient, τ_{ij} is an additional stress associated to the microstructure, also called
280 the microstress, and Σ_{ijk} is the double stress dual of the virtual micro second gradient. Furthermore, \bar{t}_i is the classical external traction force per unit area, \bar{T}_i is an additional external double force per unit area, both applied on a part Γ_σ^t of the boundary of Ω^t . Du_i^* is the normal derivative of u_i^* and is given as $Du_i^* = \frac{\partial u_i^*}{\partial x_k^t} n_k^t$, where n_k^t is the normal unit vector to the boundary.

285 An additional constitutive law has to be defined for the double stress. Σ_{ijk} is assumed to be independent of the pore water pressure and only a little information is available on the relation existing between this stress and the micro-deformation. A linear elastic mechanical law is chosen for simplicity reason with the purpose of introducing as few additional parameters as possible. It consists
290 of an isotropic linear relationship deduced from Mindlin (1965) that gives the Jaumann double stress rate $\dot{\tilde{\Sigma}}_{ijk}$ as a function of the micro second gradient rate \dot{h}_{ijk} (Collin et al., 2006). It depends on only one constitutive elastic parameter D that represents the physical microstructure and that is related to the internal length scale relevant for the shear band width (Chambon et al., 1998; Kotronis

295 et al., 2007; Collin et al., 2009a).

In order to obtain a local second gradient continuum medium, the microkinematic gradient is equal to the macrodeformation gradient $v_{ij} = F_{ij}$, leading to :

$$v_{ij}^* = F_{ij}^* = \frac{\partial u_i^*}{\partial x_j^t} \quad (55)$$

for the virtual fields. Moreover, to implement the balance equation of Eq. 54 in a finite element code, the displacement field has to be a continuously differentiable function (class C^1 function whose derivative is continuous) because second order derivatives of the displacement field are involved (Zervos et al., 2001b). To
 300 fulfil this requirement, the kinematic restriction of Eq. 55, is introduced in the momentum balance equation through a field of Lagrange multipliers λ_{ij} (Chambon et al., 1998) :

$$\int_{\Omega^t} \left(\sigma_{ij}^t \frac{\partial u_i^*}{\partial x_j^t} + \Sigma_{ijk}^t \frac{\partial v_{ij}^*}{\partial x_k^t} - \lambda_{ij}^t \left(\frac{\partial u_i^*}{\partial x_j^t} - v_{ij}^* \right) \right) d\Omega^t = \int_{\Gamma_\sigma^t} (\bar{t}_i u_i^* + \bar{T}_i v_{ik}^* n_k^t) d\Gamma^t \quad (56)$$

$$\int_{\Omega^t} \lambda_{ij}^* \left(\frac{\partial u_i^t}{\partial x_j^t} - v_{ij}^t \right) d\Omega^t = 0 \quad (57)$$

The fluid mass balance equation for every kinematically admissible virtual pore water pressure field p_w^* reads :

$$\int_{\Omega^t} \left(\dot{M}_w^t p_w^* - m_{w,i}^t \frac{\partial p_w^*}{\partial x_i^t} \right) d\Omega^t = \int_{\Omega^t} Q^t p_w^* d\Omega^t - \int_{\Gamma_q^t} \bar{q}^t p_w^* d\Gamma^t \quad (58)$$

where \dot{M}_w is the water mass variation, $m_{w,i}$ is the water mass flow, Q is a water sink term and Γ_q^t is the part of the boundary where the input water mass per unit area \bar{q} is imposed. The water transfer in porous media is characterised by :

$$m_{w,i}^t = \rho_w q_{w,i}^t = -\rho_w \frac{k_{ij}}{\mu_w} \frac{\partial p_w^t}{\partial x_j^t} \quad (59)$$

where ρ_w is the fluid density, $q_{w,i}$ is the average speed of the liquid phase relative to the solid phase which is modelled by considering the advection of the

305 liquid phase by Darcy’s flow, μ_w is the water dynamic viscosity and k_{ij} is the anisotropic intrinsic hydraulic permeability tensor.

The non-linear system of the coupled finite element formulation defined by Eq. 56, 57 and 58 is solved by time discretisation and iterative procedure using a Newton-Raphson method. A first configuration Ω^t in equilibrium with the boundary conditions at a given time t and another Ω^τ not at equilibrium at the end of the time step $\tau = t + \Delta t$ are assumed. The solution at the end of the time step is guessed and therefore the non-equilibrium forces of the three considered equations, i.e. residuals, W_1^t , W_2^t and W_3^t are defined. The linearisation of the system is defined in Collin et al. (2006) and is finally rewritten in matricial form :

$$\int_{\Omega^t} \left[U_{(x,y)}^{*,t} \right]^T [E^t] \left[dU_{(x,y)}^t \right] d\Omega^t = -W_1^t - W_2^t - W_3^t \quad (60)$$

where $[E^t]$ is the stiffness (tangent) matrix. The matrices $\left[U_{(x,y)}^{*,t} \right]$, $\left[dU_{(x,y)}^t \right]$ and $[E^t]$ are detailed by Collin et al. (2006) for saturated material. $[E^t]$ is also defined by Pardoen et al. (2015a) for unsaturated conditions, anisotropic hydraulic permeability and solid grains compressibility introduced through Biot’s
 310 coefficient.

3.3. Bifurcation theory

From a theoretical perspective, the appearance of strain localisation is considered as a bifurcation phenomenon which can be defined as the loss of uniqueness of a problem solution (Hill, 1958; Rice, 1976; Chambon & Caillerie, 1999).
 315 The bifurcation can be characterised by various modes such as surface wave (Triantafyllidis, 1980), striction (Hill & Hutchinson, 1975), diffuse loss of homogeneity (Vardoulakis, 1979, 1981) or shear banding (Rice, 1976). In the present study, we only focus on the analysis of the strain localisation in shear band
 320 mode. For this mode, a criterion proposed by Rice (Rudnicki & Rice, 1975; Rice, 1976) investigates the possibility of bifurcation appearance in classical material.

Two conditions are required to fulfil the Rice bifurcation criterion. Firstly, a kinematic condition specifies the discontinuity of the velocity gradient field L_{ij} across the shear band interfaces :

$$L_{ij}^1 = L_{ij}^0 + g_i n_j \quad (61)$$

where n_i is the normal vector of the shear band and g_i is an additional velocity gradient. In the Eq. 61 and in the followings, the superscripts ⁰ and ¹ denote quantities outside and inside the shear band, respectively.

Secondly, a static condition specifies the equilibrium of the shear band interfaces with the outer material and the discontinuity of the Cauchy stress field rate $\dot{\sigma}_{ij}$:

$$n_i (\dot{\sigma}_{ij}^1 - \dot{\sigma}_{ij}^0) = 0 \quad (62)$$

It implies that the interface traction increments $\dot{t}_i = \dot{\sigma}_{ij} n_j$ imposed on both sides of the shear band are equal.

In addition to the two previous conditions, a material constitutive law expressing the relationship between the stress and strain field increments remains to be introduced in the Rice bifurcation criterion. The elastoplastic constitutive law has been detailed for small strain and rotations in Eq. 2. It can be formulated as follows for large strain and rotations :

$$\dot{\sigma}'_{ij} = \mathcal{A}_{ijkl} L_{kl} \quad (63)$$

where \mathcal{A}_{ijkl} is the elastoplastic constitutive tangent tensor for large strain and rotations (Chambon, 1986; Wang, 1993) that is obtained by the modification of C_{ijkl} by the relation :

$$\mathcal{A}_{ijkl} = C_{ijmn} S_{mnkl} - A_{ijkl}^J \quad (64)$$

with S_{ijkl} and A_{ijkl}^J (Jaumann's correction) defined by Wang (1993). A first possibility of bifurcation appearance is a continuous bifurcation with continuous constitutive tensor across the shear band : $\mathcal{A}_{ijkl}^0 = \mathcal{A}_{ijkl}^1 = \mathcal{A}_{ijkl}$. However, the bifurcation is often discontinuous (Rice & Rudnicki, 1980) which means that the

material follows a plastic loading path in the band, whereas an elastic unloading path is followed outside the band. The constitutive tensor is therefore different outside and inside the shear strain localisation band : $\mathcal{A}_{ijkl}^0 = \mathcal{A}_{ijkl}^e$ and $\mathcal{A}_{ijkl}^1 = \mathcal{A}_{ijkl}$ with \mathcal{A}_{ijkl}^e the elastic component of \mathcal{A}_{ijkl} . Considering discontinuous bifurcation and introducing the expression of Eq. 61 and Eq. 63 in Eq. 62 gives :

$$n_i (\mathcal{A}_{ijkl}^1 (L_{kl}^0 + g_k n_l) - \mathcal{A}_{ijkl}^0 L_{kl}^0) = 0 \quad (65)$$

It has been demonstrated that the continuous bifurcation always precedes the discontinuous bifurcation (Rice & Rudnicki, 1980; Simo et al., 1993) thus, by assuming continuous bifurcation, non-trivial solutions ($g_i \neq 0$) are found if the acoustic tensor determinant is nil (Hill, 1958) :

$$\det(n_i \mathcal{A}_{ijkl} n_l) = 0 \quad (66)$$

The solution of this equation gives n_i and the orientation of the shear band. This is a necessary bifurcation condition in shear band mode that corresponds
330 to the first possible bifurcation, however this is not a sufficient condition for the appearance of shear band. Going further, a bifurcation analysis applied to the second gradient model (non-classical material) is proposed by Bésuelle et al. (2006). The authors indicate that the bifurcation criterion of the second gradient model is also a necessary but not sufficient condition for the localisation
335 onset and that it is met after the bifurcation criterion of the classical model. The analysis of bifurcation thus reduces to an analysis on the classical part of the constitutive model.

4. Numerical applications

Two numerical applications are modelled for a cross-anisotropic material in
340 order to highlight the effect of properties' anisotropy on shear banding appearance. Firstly, a plane-strain biaxial compression test is modelled on a small-scale material specimen and secondly, an underground gallery drilling is reproduced on a large scale.

4.1. Material parameters

345 Among the different materials that have been discussed in Section 2, the
properties of an argillaceous rock named the Callovo-Oxfordian claystone (COx)
are considered. This material is studied for underground radioactive waste
repository in France (Andra, 2005a) and *in situ* observations, especially the
anisotropic extent of the fractured zones observed around drifts excavated in
350 quasi-isotropic stress state in their sections, suggest that the Callovo-Oxfordian
claystone has a cross-anisotropic behaviour. Syntheses of the main parameters
obtained from laboratory testing and from the literature are detailed by Andra
(2005b) and Charlier et al. (2013); the used parameters are detailed in Tables 1,
2 and 3.

355 The anisotropic plastic parameters of Eq. 53 are determined from uniaxial
compression tests (Andra, 2005b; Yang et al., 2013) which results indicate that
the uniaxial compressive strength varies upon the loading orientation α . This
orientation corresponds to the angle between the compression direction (verti-
cal) and the normal to the bedding planes (Fig. 8) with $\alpha = 0^\circ$ if the loading
360 is perpendicular to them and $\alpha = 90^\circ$ if parallel. For uniaxial loading, this
angle is linked to the loading vector component l_3 by the relation $l_3 = \cos(\alpha)$.
Based on the yield criterion, uniaxial compressive strength is related to cohe-
sion and the constants of the second order microstructure fabric tensor can be
calculated (\bar{c} , A_{\parallel} and b_1 in Table 2, $b_2 = 0$ as well as higher order terms). The
365 evolution of the cohesion with orientation is illustrated in Fig. 7 with a mini-
mum value about $\alpha = 45^\circ$ which is consistent with experimental observations
on other cross-anisotropic argillaceous rock (Niandou et al., 1997; Valès et al.,
2004). Moreover, the influence of the cohesion anisotropy amplitude on the
shear banding appearance will be discussed in the numerical modelling.

370 The softening material behaviour has to be defined to allow the reproduc-
tion of shear banding. Small-scale compression laboratory experiments have
been discussed in Section 2.1. The results indicate the predominant role of
shear bands and fractures in the post-peak regime. Considering the material as
homogeneous, the peak stress and post-peak behaviour can be represented by

Table 1: Elastic mechanical parameters.

Symbol	Name	Value	Unit
E_{\parallel}	Parallel Young's modulus	5000	MPa
E_{\perp}	Perpendicular Young's modulus	4000	MPa
$G_{\parallel\perp}$	Shear modulus	1630	MPa
$\nu_{\parallel\parallel}$	Poisson's ratio	0.24	—
$\nu_{\parallel\perp}$	Poisson's ratio	0.33	—
b_{\parallel}	Parallel Biot's coefficient	0.60	—
b_{\perp}	Perpendicular Biot's coefficient	0.64	—
ρ_s	Solid grains density	2750	kg/m^3

Table 2: Plastic mechanical parameters.

Symbol	Name	Value	Unit
η	Yield surface convexity parameter	-0.229	—
\bar{c}	Cohesion for isotropic loading	4.1	MPa
A_{\parallel}	Cohesion parameter	0.117	—
b_1	Cohesion parameter	14.24	—
$\varphi_{c,0}$	Initial compression friction angle	10	$^{\circ}$
$\varphi_{c,f}$	Final compression friction angle	23	$^{\circ}$
$\varphi_{e,0}$	Initial extension friction angle	7	$^{\circ}$
$\varphi_{e,f}$	Final extension friction angle	23	$^{\circ}$
B_{φ}	Friction angle hardening coefficient	0.001	—
dec_{φ}	Friction angle hardening shifting	0	—
$\psi = \psi_c = \psi_e$	Dilatancy angle	0.5	$^{\circ}$

Table 3: Hydraulic parameters.

Symbol	Name	Value	Unit
k_{\parallel}	Parallel intrinsic water permeability	4×10^{-20}	m^2
k_{\perp}	Perpendicular intrinsic water permeability	1.33×10^{-20}	m^2
Φ	Porosity	0.173	—

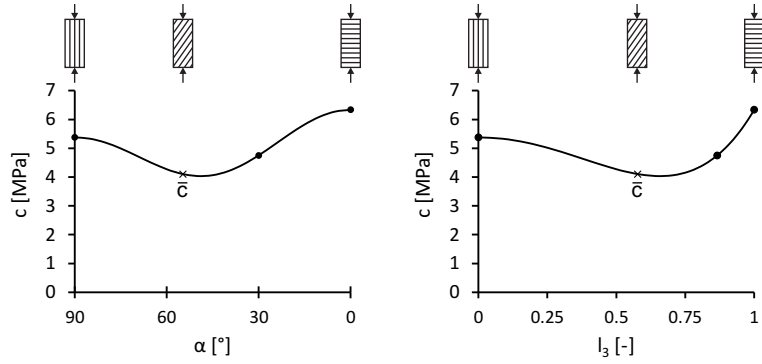


Figure 7: Evolution of the cohesion as a function of the angle between the normal to bedding planes and the direction of loading (left) and as a function of the loading vector (right).

375 strength parameters softening (cohesion for instance) in the constitutive model.
However, we propose to numerically predict the fracturing process with shear
strain localisation. The global post-peak (post-localisation) response of the
material therefore depends on the strain localisation process and its calibra-
tion requires information about the shear banding structure. More particularly,
380 shear bands pattern, orientations, number, thickness and evolution would be
necessary. Unfortunately, such information is rarely available, especially for
rocks.

Nevertheless, the strain localisation has to be triggered to model shear band-
ing. It is well known that a softening behaviour provides the conditions for strain
385 localisation and may instigate an infinity of localised solutions with non-uniform
strain distributions (Bazant et al., 1984; Benallal & Marigo, 2007; Jirásek & Rol-
shoven, 2009). The softening parameters values (ξ , B_c and dec_c) of both small
and large-scale problems are therefore chosen for that purpose. They will be
defined later for the two numerical applications.

390 The second gradient elastic modulus D has also to be characterised to prop-
erly represent the shear bands. As mentioned in Section 3.2, the internal length
scale inherent to the second gradient mechanical law is related to this consti-
tutive parameter. The value of D should be evaluated based on experimental
measurements of shear band thickness for the considered material. From a
395 modelling point of view, plenty of numerical results for second gradient media
indicate that the localisation characteristics are mesh-independent (Collin et al.,
2006). Nonetheless, a better numerical precision of the post-localisation plastic
behaviour within the bands is obtained if a few elements (at least three) com-
pose the shear band width. This remark is valid for any regularisation technique
400 including second gradient model but also gradient plasticity and non-local for-
mulation. Two values of $0.5 N$ and $5000 N$ are used for the compression test
and for the gallery excavation, respectively.

4.2. Modelling of biaxial compression test

A plane-strain biaxial compression test under undrained condition is numerically reproduced to highlight the effects of anisotropy and understand the appearance of shear strain localisation in a small material specimen. Various studies have already been performed for this type of loading, from laboratory testing to numerical modelling (Han & Drescher, 1993; Finno et al., 1997; Collin et al., 2006; Bésuelle et al., 2006; Tejchman et al., 2007).

4.2.1. Numerical model

The representation of the hydro-mechanical model under undrained condition is detailed in Fig. 8. The considered sample has a height of 50 mm and a width of 20 mm, water flow are blocked to a value of zero along the sample boundaries which makes them impervious and a constant confining pressure is applied. Experimental studies indicate that high confinement delays the appearance of strain localisation and therefore implies a larger vertical deformation and a higher peak stress to reach the localisation appearance (Mokni & Desrues, 1999). Nonetheless, the investigation of different confinements is not treated in this work and only one confinement pressure of $\sigma_x = 6 \text{ MPa}$ is considered.

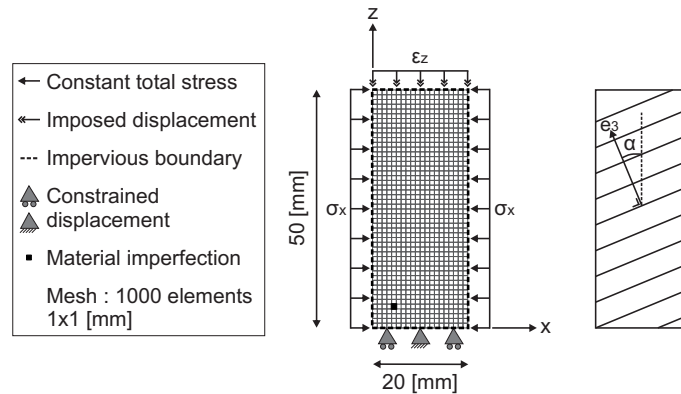


Figure 8: Numerical model used for the modelling of a plane-strain biaxial compression test performed on a cross-anisotropic rock.

To model the vertical compression, the vertical displacement of all nodes

of the sample's upper surface is progressively increased during the test with a constant loading strain rate of $1 \times 10^{-6} \text{ s}^{-1}$ up to 1.5 mm, which corresponds to a total vertical strain of $\epsilon_z = 0.03$. The vertical displacement of all nodes of the bottom surface is blocked and the displacement of the central node is blocked
 425 both in the vertical and horizontal direction to avoid rigid body displacement. When cross-anisotropy is considered, the orientation of the material isotropic planes is defined by the angle α between the vertical loading direction and the normal to the isotropic planes. This angle corresponds to the Euler's angle in the rotation matrix of Eq. 13.

430 The cohesion softening parameters are a ratio of cohesion softening of $\xi = 2$, a cohesion softening coefficient of $B_c = 0.03$ and a cohesion softening shifting of $dec_c = 0.011$. This shifting permits to delay the appearance of strain localisation and of the peak stress in the global stress-strain response curve of the specimen. Although cohesion softening is considered, strain localisation is
 435 not automatically triggered in a small material sample subjected to a biaxial compression. To ease the localisation onset, a material imperfection is included in the specimen and consists of an element (Fig. 8) having a constant cohesion of $\bar{c} = 4.1 \text{ MPa}$ (Table 2). The role of imperfection was experimentally investigated by Desrues (1984) and Desrues & Viggiani (2004) who concluded that
 440 an imperfection, be it hard or weak, does not affect the global stress-strain responses of the specimen during a biaxial plane-strain compression for the same confining pressure.

4.2.2. Anisotropy effect and strain localisation

Because a low elastic anisotropy is considered, it has only a small influence
 445 on the global reaction of a specimen biaxially loaded. Therefore we consider a cross-anisotropic elasticity with horizontal isotropic planes ($\alpha = 0^\circ$) and we investigate the effect of plastic anisotropy. The evolution of the global deviatoric stress $q = \sigma_z - \sigma_x$ with the vertical strain ϵ_z is detailed in Fig. 9 for an isotropic ($c_0 = 4.1 \text{ MPa}$, $A_{\parallel} = b_1 = 0$) and an anisotropic plasticity ($c_0 = 4.1 \text{ MPa}$,
 450 $A_{\parallel} = 0.117$ and $b_1 = 14.24$ from Table 2). The homogeneous solution without

cohesion softening ($\xi = 1$) and the localised solution are detailed for both cases.

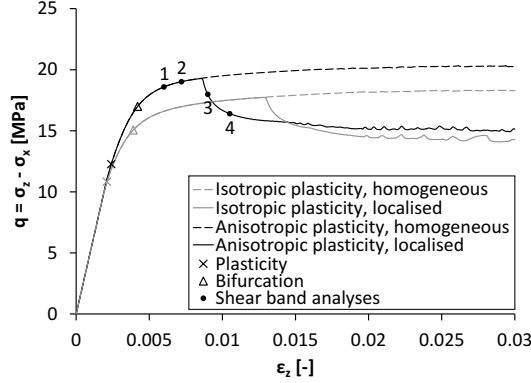


Figure 9: Stress-strain curve for isotropic and cross-anisotropic plasticity with horizontal isotropic planes.

For the homogeneous solutions, the material is initially in an elastic state up to a deformation where plasticity is observed all over the specimen which corresponds to the crosses on the stress-strain curves. In the plastic domain, the increase of the deviatoric stress is due to the friction angles hardening. If we compare the isotropic and anisotropic homogeneous solutions, one can observe an increase of the material global resistance due to the anisotropy of the cohesion and its evolution during the loading. When the isotropic planes are horizontal and an isotropic confinement followed by a vertical loading is applied, the global loading tends to be more and more perpendicular to the bedding. In this case the cohesion evolves from its original value \bar{c} , corresponding to an isotropic loading with loading vector component $l_3 = \sqrt{1/3} = 0.58$, towards the right hand side of the curve detailed in Fig. 7. The evolution of the cohesion in the specimen can be described more accurately by studying one element (element 1 in Fig. 12). We only need to analyse one element so far because the considered solutions are homogeneous and the evolutions of its cohesion, loading vector and yield index are represented in Fig. 13. The increases of cohesion is clearly noticeable when anisotropy is taken into account because the loading vector component l_3 increases from 0.58 to 0.88 during the loading, which affects the

cohesion value (Eq. 53). The yield index is defined as the reduced deviatoric stress invariant :

$$YI = \frac{II_{\hat{\sigma}}}{II_{\hat{\sigma}}^p} \quad (67)$$

where $II_{\hat{\sigma}}$ is the second deviatoric stress invariant of Eq. 24 and $II_{\hat{\sigma}}^p$ is the second deviatoric stress invariant value for which the material enters plastic state for an identical value of the first stress invariant $I_{\sigma'}$ (current value). The
 455 yield index is then equal to one in the plastic domain and is lower than one in the elastic domain. One can observe in Fig. 13 for the homogeneous solutions that the material becomes rapidly plastic and remains plastic up to the end of the loading whether cross-anisotropic plasticity is taken into account or not.

To trigger strain localisation the cohesion softening ($\xi = 2$, $B_c = 0.03$ and
 460 $dec_c = 0.011$) and the material imperfection are added to the previous modelling. The evolution of the global deviatoric stress with the vertical strain (Fig. 9) exhibits different zones : an elastic zone, a pre-peak plastic zone without reaching the bifurcation criterion, a pre-peak plastic zone where the bifurcation criterion is reached and a post-peak plastic zone. In homogeneous plastic
 465 state, the friction angle increases due to hardening before the peak stress is reached. The possibility of localisation occurrence is then derived from the solutions of the characteristic equation of the bifurcation criterion (Eq. 66). For associated plasticity the bifurcation criterion is only met at peak stress but for non-associated plasticity it can be met for positive hardening and shear band-
 470 ing can occurs in the hardening regime (Rudnicki & Rice, 1975). The pre-peak hardening plastic regime can thus be divided in two parts : one in which the bifurcation criterion is not reached and another where it is reached all over the specimen (after the triangles on the stress-strain curves) and where strain localisation can initiate even if the specimen still remains homogeneously plastic
 475 (continuous bifurcation).

In order to understand the evolution of the shear band activity during the biaxial loading, different shear band analyses are performed for the anisotropic case. Theses analyses are indicated with dots on the stress-strain curve of Fig. 9

and are detailed in Fig. 10 where the deviatoric strain increment, the plastic zone, the nodal velocity norm and the pore water pressure are illustrated. The deviatoric strain increment represents the band activity and is defined by :

$$\kappa = \frac{\dot{\hat{\epsilon}}_{eq} dt}{\int \dot{\hat{\epsilon}}_{eq} dt} \quad (68)$$

where $\hat{\epsilon}_{eq}$ is Von Mises' equivalent deviatoric total strain, i.e. total deviatoric strain :

$$\hat{\epsilon}_{eq} = \sqrt{\frac{2}{3} \hat{\epsilon}_{ij} \hat{\epsilon}_{ij}} \quad (69)$$

where $\hat{\epsilon}_{ij} = \epsilon_{ij} - \frac{\epsilon_{kk}}{3} \delta_{ij}$ is the deviatoric total strain field calculated from the total strain tensor ϵ_{ij} . The plastic zone represents the plastic loading integration points (red squares) and the nodal velocity norm corresponds to the norm of the nodal displacement rates $\|v\| = \sqrt{\dot{u}_x^2 + \dot{u}_z^2}$. The velocity is represented on the deformed mesh and the global movements in the specimen are indicated with arrows.

The analyses of shear band once the bifurcation is reached but before the peak stress can be observed for $\epsilon_z = 0.0060$ (1) and $\epsilon_z = 0.0075$ (2) in Fig. 10. The results in terms of deviatoric strain increment indicate clearly that different shear bands appear and are in competition at this stage. However, the plasticity remains homogeneous and the velocity norms are globally directed downwards which indicate that these shear bands are not fully formed yet. Furthermore, the imperfection dictates the shear band position which passes through it. In fact, the stress field is uniform for a uniform specimen and the bifurcation criterion is reached simultaneously in the whole specimen. On the other hand, an imperfection induces a non-uniformity of the stress field in its vicinity which can be sufficient to reach first the bifurcation criterion (only in the imperfection) and then the material imperfection acts as a nucleation point for the strain localisation onset.

Once the cohesion softening starts, one of the shear band outweighs the others and fully develops. The peak stress corresponds then to the appearance of a fully formed shear band throughout the specimen. The full formation

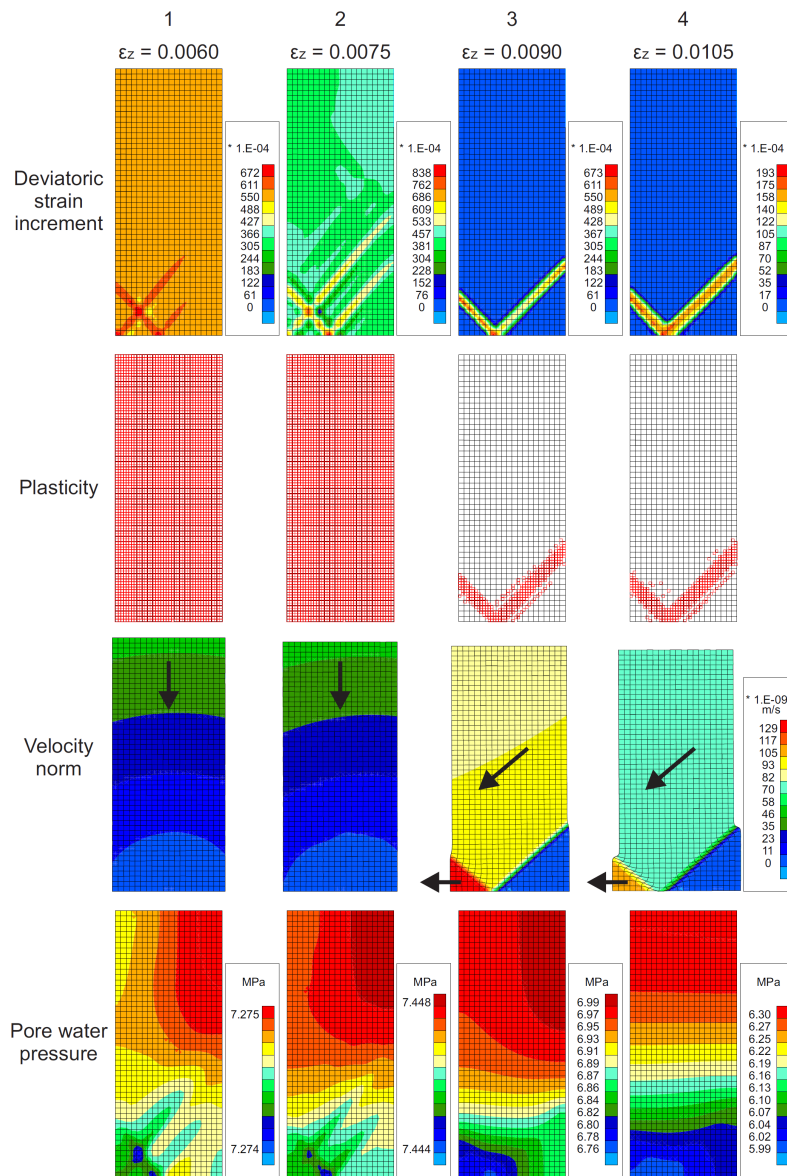


Figure 10: Appearance of strain localisation before peak stress and complete formation of a shear band after peak stress for cross-anisotropic material with horizontal isotropic planes.

of the shear band can be observed in Fig. 10 for $\epsilon_z = 0.0090$ (3) and $\epsilon_z = 0.0105$ (4) by the concentration of deviatoric strain and plasticity inside the shear band. After the peak, a rapid drop of the deviatoric stress is observed (Fig. 9) due to the cohesion softening and to the elastic unloading of the elements located outside the shear band, the elements inside the band remain plastic. As already mentioned, the strain softening behaviour (reduction of shear stress with increase of plastic strain) causes a loss of uniqueness of the post-peak solution due to the possible elastic unloading. An infinity of localised solutions with non-uniform strain distributions may occur at the peak stress bifurcation point and this non-uniqueness issue is addressed by the inclusion of the material imperfection. Further, the strong decrease of the specimen global reaction is followed by a plateau with a quasi-constant stress value.

The same type of shear strain localisation results have been obtained experimentally by Desrues (1984) and Desrues & Viggiani (2004) for many biaxial compression tests. One example of shear band development in sand is represented in Fig. 11 where the stress-strain curve and the incremental fields of shear strain intensity based on stereophotogrammetry are represented before and after the peak. The experimental results also indicate that strain localisation initiates before the peak stress, generally at simultaneous multiple locations within a large part of the specimen. These multiple mechanisms of localised deformation observed experimentally are temporary because they are in competition as the deformation increases and finally one of them takes over the others at peak stress to complete a full formation of a shear band throughout the specimen. The authors also investigate the role of imperfection, be it hard or weak, in a given specimen. Two main observations were made : first, the imperfection does not affect neither the global stress-strain response of the specimen nor the peak stress and strain level, second, the shear band position is dictated by the inclusion and passes through it (if the imperfection is strong enough) which is confirmed by the numerical results.

As mentioned in Section 2.1, only a few experimental analyses of shear strain localisation are available for rocks like the Callovo-Oxfordian claystone. Besides,

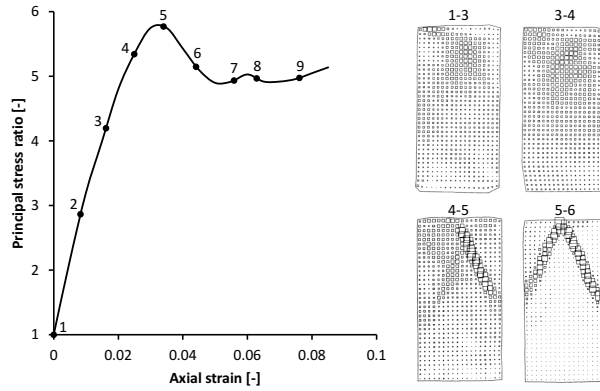


Figure 11: Stress-strain curve and incremental fields of shear strain intensity based on stereophotogrammetry in sand from Desrues & Viggiani (2004).

the resaturation conditions are generally not the same as the ones of the de-
 530 veloped modelling, consequently comparison is not straightforward and only
 qualitative comparisons are proposed in the present study.

Going back to the numerical results, the shear strain localisation band ex-
 hibits a reflexion on the bottom surface of the sample therefore the material
 is divided in three zones or blocks with different types of movements (see the
 535 nodal velocity norm in Fig. 10). Firstly, the bottom right zone is blocked due to
 the constrained displacements in both directions imposed on the central node
 of the bottom surface. Secondly, the major central zone is pushed downwards
 and slides along the bottom right zone in the bottom left direction. Lastly, the
 bottom left zone can only move in the left direction because it is blocked in the
 540 vertical direction. The same types of block displacements along the shear bands
 are observed on experimental results (Desrues & Viggiani, 2004).

Fig. 10 also illustrates the evolution of the pore water pressure during the
 localisation process. Initially, the pore pressure is nil in the sample, then it
 evolves during the loading and a uniform variation is expected under undrained
 545 condition. As long as the deformation is uniform within the sample, the pore
 pressure remains uniform as well. Once strain localisation and non-uniformity
 appear, one can observe a slight variation of pore pressure across the sample.

Before the peak stress ($\epsilon_z < 0.0086$), the pressure remains quasi-uniform and globally increases. After the peak stress, a vertical gradient tends to appear
 550 with lower values in the localised zone that may be due to dilatancy effect. The material dilatancy angle is very low ($\psi = 0.5^\circ$ in Table 2) so such phenomenon should be limited, nevertheless it can also be due to the kinematics related to localisation process. Nonetheless, the pore pressure variations remain low across the whole sample.

555 Moreover, as the results of Fig. 9 indicate, the peak amplitude q and position ϵ_z of the localised solutions are different when plastic anisotropy is taken into account. The peak resistance of the specimen is higher when considering cohesion anisotropy and the global vertical deformation required to reach this peak is lower. This is due to the homogeneous evolution of the specimen cohesion before the peak stress (Fig. 13). After the peak stress ($\epsilon_z > 0.0086$), the evolution of cohesion is not homogeneous anymore and, consequently, different elements in the specimen have to be analysed to capture this non-homogeneous evolution. The three elements of Fig. 12 have been chosen : element 1 is the same central element as considered for the homogeneous solutions and is located
 560 outside the shear band, element 2 is located inside the shear band and element 3 is located on the interface between the shear band and the outer material. The evolution of cohesion, loading vector and yield index of those three elements are detailed in Fig. 13.

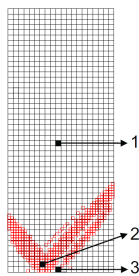


Figure 12: Elements chosen for the analysis of cohesion evolution during biaxial compression test.

The element 1 is located outside the shear band and does not remain plastic

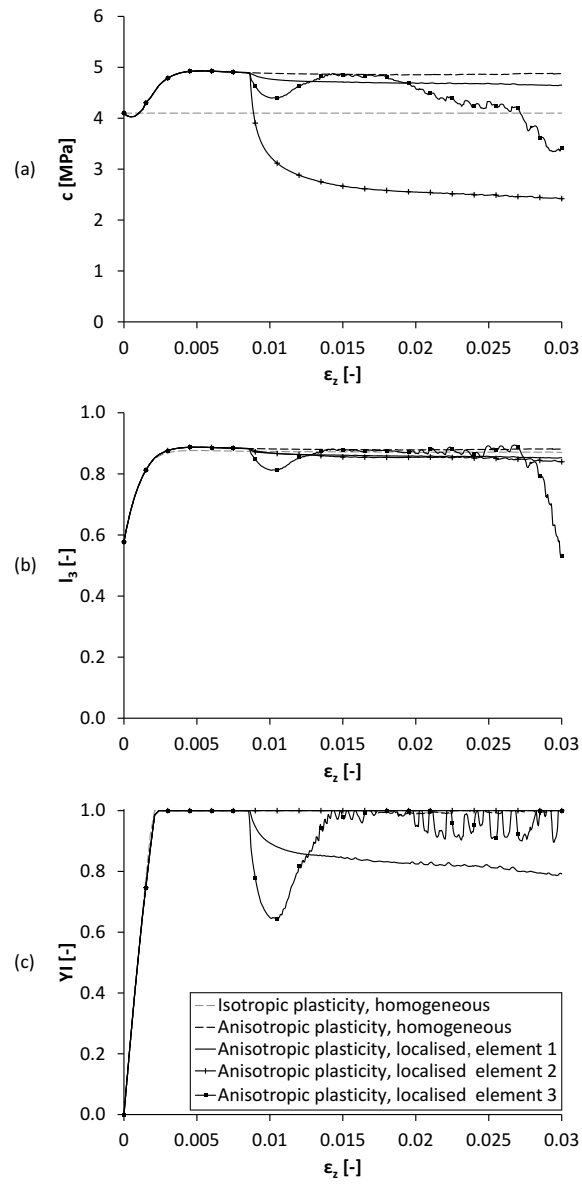


Figure 13: Cohesion (a), loading vector (b) and yield index (c) evolutions for isotropic and cross-anisotropic plasticity with horizontal isotropic planes.

570 after it fully develops. Plastic deformation is not accumulated after the peak
 stress because of this elastic unloading and the cohesion only decreases a little
 regarding the homogeneous solution due to the modification of loading orienta-
 tion (l_3 slightly decreases after the peak) and to the cohesion anisotropy. The
 element 2 is located inside the shear band and remains plastic which engen-
 575 ders an accumulation of plastic deformation and a strong cohesion decrease due
 to softening. A slight part of the cohesion decrease is still due to the cohe-
 sion anisotropy then the cohesion is affected by material softening as well as
 anisotropic characteristics. For the element 3, the cohesion evolves quite differ-
 ently than for the two other elements. Matter of fact, this element is located
 580 at the interface between the shear band and the outer material but the position
 of this interface is not fixed during the loading, it slightly evolves due to the
 band activity. Then, the element 3 can be located inside or outside the shear
 band which implies plastic or elastic state and an intermittent accumulation of
 plastic strain causing cohesion softening. Besides this, the stress state and the
 585 loading vector component l_3 evolve in element 3 after the full development of
 the shear band which modify the cohesion due to its anisotropy. As for element
 2, material softening and anisotropy contribute to the cohesion evolution.

4.2.3. *Isotropic planes rotation*

To highlight the effect of cross-anisotropy, the biaxial compression can be
 590 performed for different orientations of the isotropic planes. For $\alpha = 45^\circ$ we
 obtain the stress-strain curve and the shear band pattern evolution detailed
 in Fig. 14 and Fig. 15, respectively. Different shear band analyses are again
 realised for different vertical deformations during the biaxial loading, they are
 indicated with dots on the stress-strain curve. As previously observed, strain
 595 localisation appears before the peak stress when the bifurcation criterion is met
 ($\epsilon_z = 0.0075$ (1)) and one shear band fully develops once the peak stress is
 reached ($\epsilon_z = 0.0090$ (2)). In comparison with the loading of a specimen having
 horizontal isotropic planes, the results are globally the same except that the
 pattern of strain localisation at its onset varies, the peak stress value is lower

600 and the post-peak behaviour exhibits variations of the deviatoric stress.

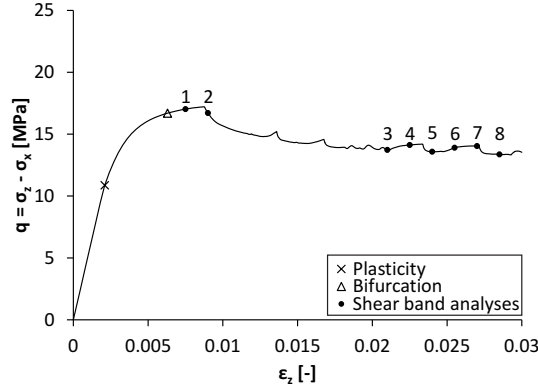


Figure 14: Stress-strain curve for cross-anisotropic plasticity with isotropic planes orientation $\alpha = 45^\circ$.

The two first differences are once more due to the anisotropy of the cohesion and its evolution during the loading (Fig. 7). In fact, when the isotropic planes are not horizontal and the vertical loading is performed, the cohesion evolves from \bar{c} towards c_α and in this case c_{45° is about the lowest cohesion value, which leads to a lower peak stress value. c_{45° is also very close to the initial cohesion value \bar{c} then the modification of cohesion in the specimen during the loading is very low and the imperfection, with its constant cohesion value of \bar{c} , is of minor importance. This minor imperfection is not strong enough to act as a strain localisation attractor and more multiple mechanisms of localised deformation appear at the onset of localisation ($\epsilon_z = 0.0075$ (1) in Fig. 15). After the competition process among the different localised structures, the shear band that outweighs the others does not pass by the imperfection. It suggests that a material imperfection has to be strong enough to act as a localisation attractor and in case of strong imperfection only one well-defined shear band passing by the imperfection could be triggered without any competition process. The same conclusions were drawn by Desrues & Viggiani (2004) based on experimental results.

The variation of the deviatoric stress in the post-peak behaviour is due to the

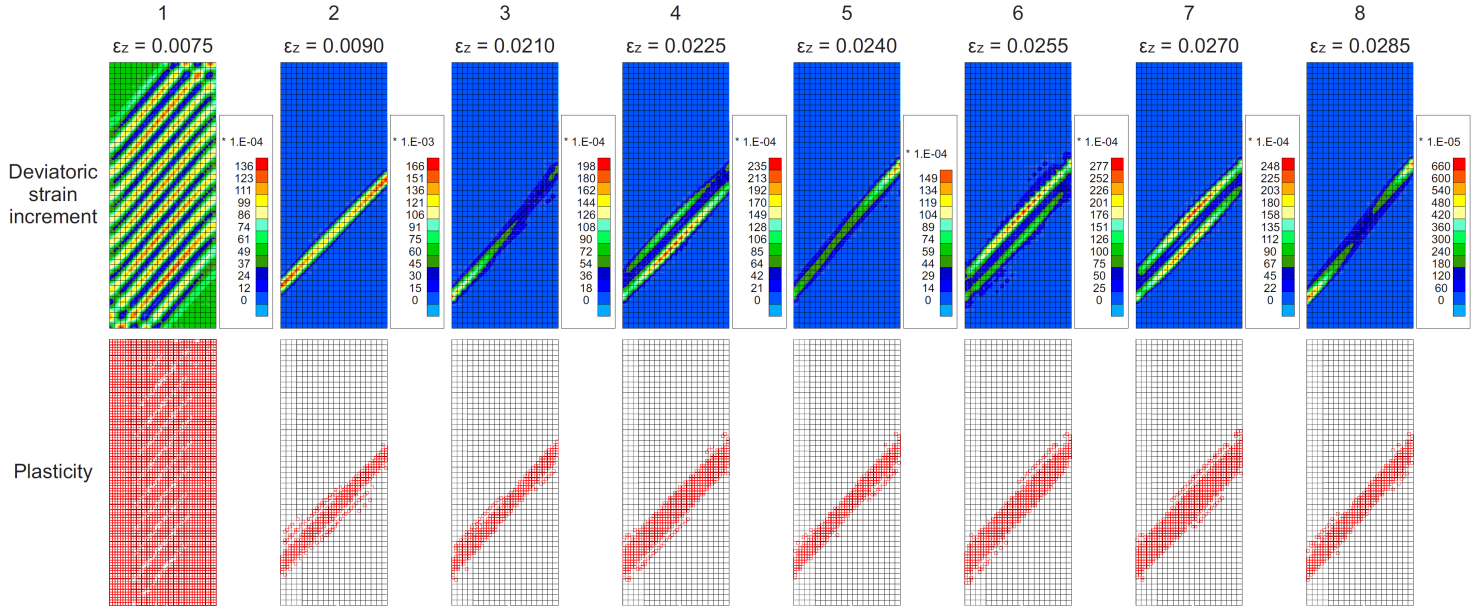


Figure 15: Characterisation of the post-localisation regime by shear band activity for cross-anisotropic material with isotropic planes orientation $\alpha = 45^\circ$.

plastic loading of the elements located inside the shear band and to the elastic
620 unloading of the elements located outside. An increase of the global response
force corresponds to an increase of the shear band activity. From $\epsilon_z = 0.0210$
(3) to $\epsilon_z = 0.0225$ (4) we observe that a second shear band appears next to
the principal one causing a slight increase of the plastic zone size and of the
specimen response. Then, a decrease of the global response force is observed
625 and corresponds to a decrease of the shear band activity. For $\epsilon_z = 0.0240$ (5) we
observe only one shear band and a slight decrease of the plastic zone size with
elastic unloading of the elements outside the shear band. The same behaviour
is observed for the other increases and decreases of the deviatoric stress (see
 $\epsilon_z = 0.0255$ (6), 0.0270 (7) and 0.0285 (8) in Fig. 15). Experimentally, a con-
630 sequent drop of the global stress response in the post-peak regime corresponds
to the emergence of a new shear band across the whole specimen (Fig. 1) which
is not observed on the numerical result for the considered material. Nonetheless,
experimental techniques such as digital image correlation have revealed the

evolution of strain localisation throughout the entire duration of the tests and
635 point out that variations of band activity as well as competition between the
emerging shear bands are observed for diverse materials (Viggiani & Desrues,
2004; Thakur, 2007).

Various orientations of the isotropic planes ranging from 0° to 90° are also
considered in order to deeper analyse the isotropic planes rotation effect and the
640 obtained stress-strain curves are detailed in Fig. 16. One can observe that the
elastic response varies in function of the elastic modulus anisotropy; E_{\parallel} being
larger than E_{\perp} in a ratio 1.25 (see Table 1) leads to a steeper slope as α increases.
Concerning the plastic response, the peak stress values evolve with the cohesion
which is the lowest around 45° (Fig. 7) and the post-peak regime is similar to
645 what has already been observed, with or without variations of the deviatoric
stress. The final shear band patterns at $\epsilon_z = 0.03$ are detailed in Fig. 17 in
terms of total deviatoric strain $\hat{\epsilon}_{eq}$. A reflexive shear band is observed on the
bottom surface of the specimen for 0° and 90° , and only one band is observed in
the middle of the specimen for the other intermediate orientations. The rupture
650 and deformation of the specimen have already been discussed through material
blocks movements in case of a reflexive shear band. For a shear band going
across the specimen, the bottom zone is blocked because of the constrained
displacements and the top block slides on it in the bottom right or left direction
depending on the orientation of the shear band. It can also be observed that the
655 position of the shear band varies with the isotropic planes orientation but not
the number of bands, neither their orientations with the horizontal direction.

4.2.4. Shear band orientation

Different theories exist about the shear band orientation based on plasticity
or bifurcation theory, a summary is presented by Desrues (1984). A first theory
660 is the maximal obliquity line of the stress vector which is a static characteristic
of the shear band and, following Coulomb's theory (Coulomb, 1773), the ori-
entation of the shear band is $\frac{\pi}{4} \pm \frac{\varphi}{2}$ with the principal directions of the total
stresses. A second theory exposed by Roscoe (1970) specifies that rupture lines,

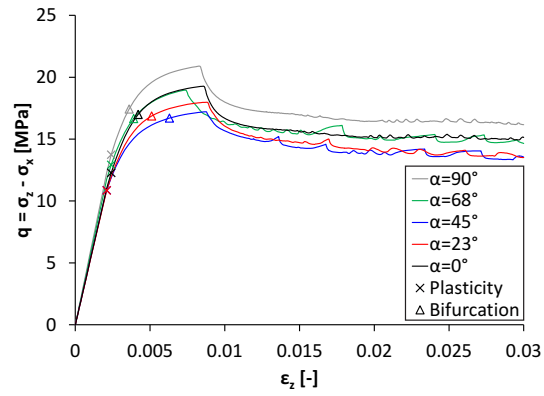


Figure 16: Stress-strain curve for cross-anisotropic material with isotropic planes orientations ranging from $\alpha = 0^\circ$ to 90° .

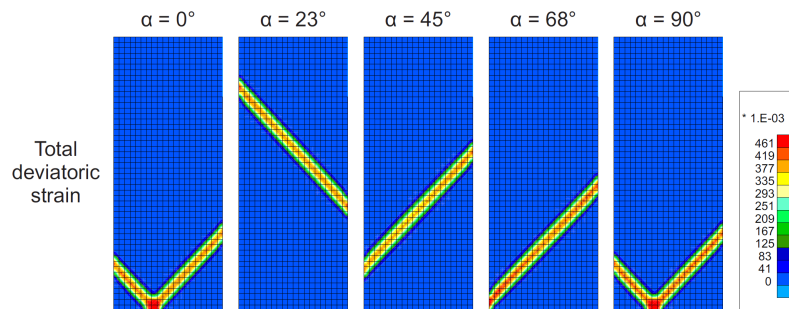


Figure 17: Shear band patterns for cross-anisotropic material with isotropic planes orientations ranging from $\alpha = 0^\circ$ to 90° .

i.e. the sheared planes, are zero extension lines. The zero extension condition is
 665 a kinematic characteristic of the shear band implying that the rupture surface
 has an indefinite length and no longitudinal deformation (Desrues, 1984, 1987).
 Following this condition, the shear band orientation is $\frac{\pi}{4} \pm \frac{\psi}{2}$ with the principal
 directions of the strain rate. Arthur et al. (1977b) and co-workers proposed
 that the orientation of the shear band can varies within a certain range defined
 670 by the two previous orientation values and that an intermediate value $\frac{\pi}{4} \pm \frac{\varphi+\psi}{4}$
 introducing the influence of the dilatancy angle can be assumed in some cases.
 Similar conclusions based on the bifurcation theory are formulated by other
 authors such as Vardoulakis (1980) who indicates that the previous orientation
 assumed by Arthur et al. (1977b) is valid with φ and ψ at peak stress value
 675 (bifurcation).

The definition of the two sets of conjugated shear band orientations Θ with
 respect to the minor principal stress can thus be summarised as follows :

$$|\Theta_R| \leq |\Theta| \leq |\Theta_C| \quad (70)$$

where Θ_C and Θ_R are Coulomb's and Roscoe's angle, respectively :

$$\Theta_C = \pm \left(\frac{\pi}{4} + \frac{\varphi_{bif}}{2} \right) \quad (71)$$

$$\Theta_R = \pm \left(\frac{\pi}{4} + \frac{\psi_{bif}}{2} \right) \quad (72)$$

These definitions are principally valid for perfectly-plastic models. In case of
 hardening non-associated plasticity, the strain localisation can initiate in the
 hardening phase before reaching the peak stress and a unique pair of shear bands
 exists for an intermediate orientation value of about (Mehrabadi & Cowin, 1980;
 Anand, 1983; Shuttle & Smith, 1988) :

$$\Theta_A = \pm \left(\frac{\pi}{4} + \frac{\varphi_{bif} + \psi_{bif}}{4} \right) \quad (73)$$

These orientations of the shear band depend on the local behaviour at the initi-
 ation of strain localisation which corresponds to the bifurcation state (Desrues,

1984). They are therefore defined with φ_{bif} and ψ_{bif} which are the mobilised friction and the dilatancy angles at the bifurcation state.

680 The orientation of the shear band Θ provided by the numerical results can be related to the orientations discussed here above. The angles are defined with respect to the minor principal stress direction which is oriented horizontally during the biaxial compression. The observed orientation for the localised results with horizontal isotropic planes ($\alpha = 0^\circ$) is about $\Theta = 47^\circ$ and, even
685 if anisotropic parameters are included in the model, this orientation does not depend on them. At bifurcation state, $\varphi_{bif} = 17.5^\circ$ (inside the shear band when it is initiated) and $\psi_{bif} = \psi = 0.5^\circ$ which give $\Theta_R = 45.3^\circ$, $\Theta_A = 49.5^\circ$ and $\Theta_C = 53.8^\circ$. The numerical results lie between the lower bound of Roscoe's angle Θ_R and the intermediate value Θ_A . Other values of dilatancy angle are
690 investigated and lead to a modification of the shear band orientation as illustrated in Fig. 18. The evolution of φ_{bif} , Θ_R , Θ_A , Θ_C as well as the evolution of the shear band orientation obtained numerically Θ is detailed in Fig. 19 for the considered dilatancy angles. The numerical results highlight that the shear band orientation increases with the dilatancy angle and that it is close to Θ_R
695 for low values of ψ and close to Θ_A for higher values.

The orientation obtained by considering bifurcation theory can also be investigated. The solution of Eq. 66 gives the components of the normal vector of the shear band and therefore its orientation with the isotropic planes which are horizontal in this case. The shear band directions at the end of the compression
700 test are detailed in Fig. 18 with an enlargement for two elements located on different parts of the band. The orientations obtained by the bifurcation criterion indicate that shear band can initiate in two conjugate directions at every material point but only one shear band fully develops at the global specimen scale. Moreover, these orientations on each element correspond to the global
705 shear band direction.

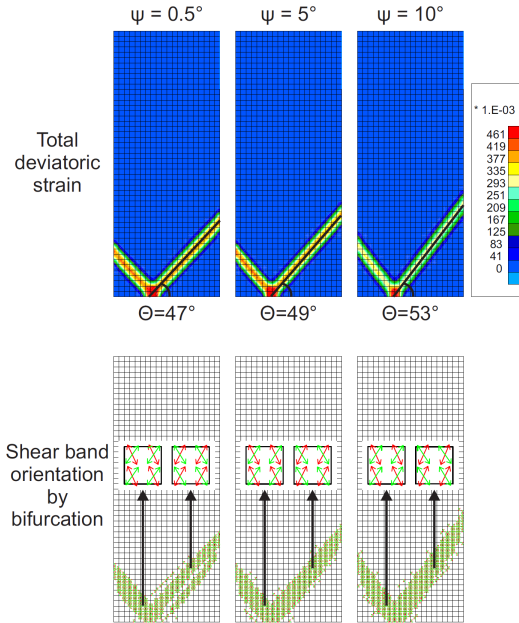


Figure 18: Evolution of shear band patterns and orientations with dilatancy angle at the end of the compression test for cross-anisotropic material with horizontal isotropic planes.

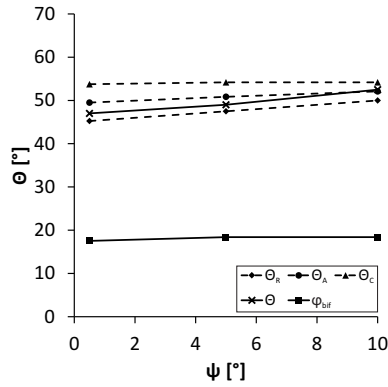


Figure 19: Evolution of shear band orientation with dilatancy angle for cross-anisotropic material with horizontal isotropic planes.

4.3. Modelling of gallery drilling

The modelling of a gallery drilling in rock is performed in two-dimensional plane-strain state with hydro-mechanical coupling. The main objective is once more to highlight the effects of material anisotropy on the appearance of shear strain localisation at large scale, around an underground gallery. A particular
710 attention is paid to the development of the excavation fractured zone due to material anisotropy with initial isotropic stress state.

4.3.1. Numerical model

A cross-anisotropic rock exhibiting horizontal bedding planes ($\alpha = 0^\circ$) and an initial isotropic stress state are considered in order to highlight the effect of material anisotropy on the development of shear bands around the gallery :

$$\sigma_{x,0} = \sigma_{y,0} = \sigma_{z,0} = 12 \text{ MPa}$$

$$p_{w,0} = 4.7 \text{ MPa}$$

where $\sigma_{x,0}$, $\sigma_{y,0}$, $\sigma_{z,0}$ are the initial total stresses and $p_{w,0}$ is the initial pore wa-
715 ter pressure. The numerical model of a 2.6 meter radius gallery is schematically represented in Fig. 20 with the mesh structure and the boundary conditions. Only one gallery quarter is discretised by assuming symmetry along the x- and z-axes with a mesh extension of 50 meters in both directions. The discretization is realised with a total of 4880 elements, 19521 nodes and a more refined
720 discretization close to the gallery.

Concerning the boundary conditions, the initial pore water pressure and stresses are imposed constant at the mesh external boundaries. The normal displacements and the water flow are blocked to zero along the symmetry axes (impervious axes) in order to establish the symmetry. Furthermore, a higher order kinematic boundary condition has to be considered to establish the symmetry (Zervos et al., 2001a) due to the existence of gradient terms in the equilibrium equations of the second gradient model. It comes in addition to the classical boundary condition on the normal displacements. This constraint requires a symmetric radial displacement u_r on both sides of the symmetry axes, implying

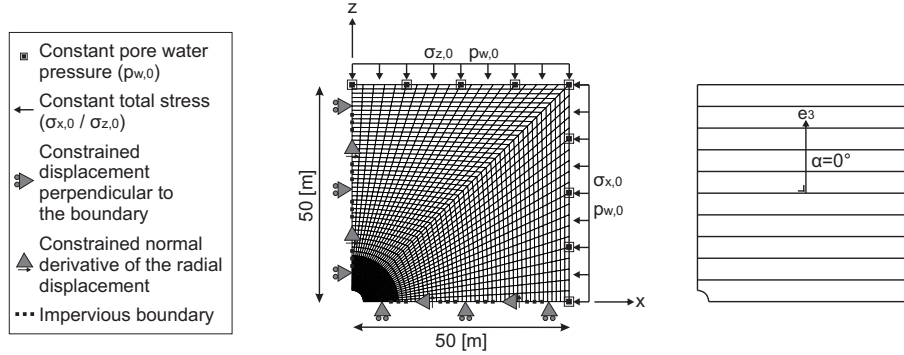


Figure 20: Numerical model used for the modelling of a gallery excavation in a cross-anisotropic rock with horizontal bedding planes.

the cancellation of its normal derivative with respect to the tangential direction ϑ :

$$\frac{\partial u_r}{\partial \vartheta} = 0 \quad (74)$$

which is equivalent to :

$$x - axis : \frac{\partial u_x}{\partial z} = 0 \quad (75)$$

$$z - axis : \frac{\partial u_z}{\partial x} = 0 \quad (76)$$

where u_x and u_z are the horizontal and vertical displacements, respectively.

Now that the initial state, the geometry and the boundary conditions are defined, the gallery excavation can be characterised. It is performed with the convergence-confinement method which is an approximation method for tunnelling that allows to transform a whole three dimensional study of tunnel excavation in a two dimensional study in plane-strain state (Bernaud & Rousset, 1992), based on an identical gallery convergence assumption. The effect of the excavation front progress is taken into account by applying a fictive pressure σ_r^Γ on the gallery wall that depends on the proximity of the excavation front to the studied gallery section, as detailed in Fig. 21. A deconfinement rate ζ ranging from 0 to 1 is defined by Panet & Guellec (1974) :

$$\sigma_r^\Gamma = (1 - \zeta) \sigma_{r,0} \quad (77)$$

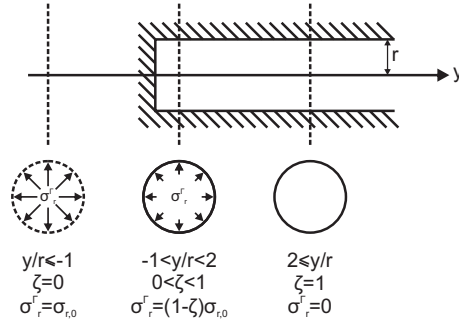


Figure 21: Deconfinement rate during gallery excavation by Panet & Guenot (1982).

where $\sigma_{r,0}$ is the initial pressure on the gallery wall that corresponds to the initial isotropic stress in the material.

The deconfinement rate depends on various parameters and its analytical
725 determination is beyond the scope of the present study. Among different theories
(Bernaud & Rousset, 1992; Carranza-Torres & Fairhurst, 2000), we use the
deconfinement curve given by Panet & Guenot (1982) and detailed in Fig. 22
where $1 - \zeta$ depends on the ratio of the distance between the excavation front
and the studied section y by the gallery radius r . The deconfinement rate can
730 also be expressed as a function of time if the speed of excavation is known.
Hereafter we consider a speed of one gallery radius (2.6 m) per week implying
that the excavation front crosses the studied section after one week (7 days)
and that the excavation is fully completed after three weeks (21 days). The
evolution of the deconfinement rate with time is detailed in Fig. 22.

The decrease of pore water pressure at gallery wall p_w^Γ during the drilling
has to be considered as well because we are performing a hydro-mechanical
modelling. A deconfinement rate ζ_w can be defined in the same manner as for
the radial stress :

$$p_w^\Gamma = (1 - \zeta_w) p_{w,0} \quad (78)$$

735 where $p_{w,0}$ is the initial pore water pressure on the gallery wall that corresponds
to the initial pore water pressure in the material.

The approach of Panet & Guellec (1974) was originally validated for dry

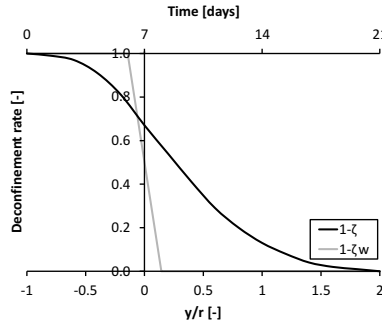


Figure 22: Deconfinement curve for the radial stress by Panet & Guenot (1982) and for the pore water pressure during gallery excavation.

isotropic materials and its generalisation to anisotropic rock under saturated conditions is not straightforward. During the drilling, pore overpressures are usually observed in the rock ahead of the excavation front and are characteristic of hydro-mechanical coupling induced by the anisotropy, whether of the stress state or of the rock mechanical behaviour. Nonetheless, for the sake of simplicity, a linear decrease of pore water pressure is assumed during the excavation (no overpressures) and a uniform deconfinement rate is considered for the total radial stress (Eq. 77). The pore water pressure is assumed to rapidly decrease when the excavation front crosses the studied section, from one day before the front up to one day after (Fig. 22). More accurate definitions of the deconfinement rates would need to be validated with three-dimensional excavation computations, nevertheless these developments are beyond the objectives of this study.

Preliminary calculations have indicated that the deformation around the gallery due to the drilling are globally lower than in a biaxial compression test. As a consequence, the introduction of a stronger cohesion softening without shifting is necessary to trigger the shear strain localisation. The softening parameters are $\xi = 5$, $B_c = 0.003$ and $dec_c = 0$.

4.3.2. Anisotropy effect and strain localisation

The onset of fractures and strain localisation around galleries depend on the material anisotropy. Previous numerical studies indicate that for an isotropic

Table 4: Anisotropic cohesion parameters for gallery excavation.

Symbol	Name	Isotrope	Anisotrope set 1	Anisotrope set 2	Anisotrope set 3	Unit
\bar{c}	Cohesion for isotropic loading	4.1	4.1	4.1	4.1	<i>MPa</i>
A_{\parallel}	Cohesion parameter	0	-0.007	0.049	0.117	-
b_1	Cohesion parameter	0	1105	50.93	14.24	-

material with an isotropic initial stress state, shear strain localisation is not triggered during the drilling. An anisotropic stress state in the plane perpendicular to the gallery axis (gallery section) is a predominant factor that can lead to the triggering of strain localisation and to the creation of the excavation fractured zone during the drilling (Collin & Pardoën, 2013; Pardoën et al., 2015a; Salehnia et al., 2015). Moreover, this fractured zone has an elliptical extension with a significantly larger extent in one direction, depending on the stress anisotropy.

Nevertheless, the development of a fractured zone has been observed in some materials even for isotropic or quasi-isotropic stress state in the gallery section (Armand et al., 2014). In this case, it seems necessary to consider the material anisotropy. To do so, the elastic cross-anisotropy is taken into account (Table 1) and, since the bifurcation criterion as well as the strain localisation can only be reached when the material is in plastic state, the plastic anisotropy is analysed through the cohesion anisotropy. Different cases are considered from an isotropic cohesion of 4.1 *MPa* to the anisotropic parameters detailed in Table 2. Two other cohesion anisotropies are considered between those two cases which leads to a total of four sets of anisotropic cohesion parameters detailed in Table 4. The evolutions of the cohesion with the loading vector component l_3 are detailed in Fig. 23.

The shear band patterns obtained at the end of the excavation in case of horizontal bedding (Fig. 20) are detailed in Fig. 24 for the different sets of parameters. The illustrated results are the total deviatoric strain, the plastic zone

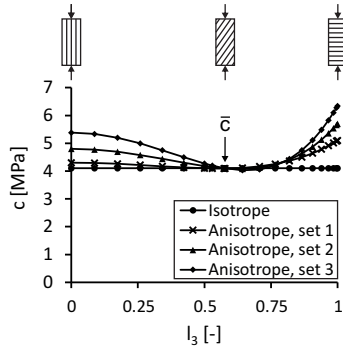


Figure 23: Various evolutions of the cohesion as a function of the loading vector.

780 and the cohesion. For the isotropic cohesion, one can observe that the deformation and the plastic zone are diffuse around the gallery with a quasi-circular extension of about one gallery radius (2.6 m) in the rock. Actually, it is slightly wider in the horizontal direction due to the elastic anisotropic properties. The plasticity engenders cohesion softening around the gallery which is also diffuse.

785 For the set 1 of anisotropic cohesion parameters, the plastic zone remains almost circular around the gallery with the same extension and the total deviatoric strain as well as the cohesion softening concentrate in an inclined direction at about 45° with the horizontal. For the set 2 of anisotropic cohesion parameters, the strain localisation is triggered during the excavation in an inclined direction and shear bands in chevron pattern develop with elastic unloading outside the bands.

790 The plasticity, the total deviatoric strain and the cohesion softening concentrate within the shear bands. For the set 3 of anisotropic cohesion parameters, the strain localisation starts earlier with the same type of shear banding pattern but with a larger number of bands, located preferentially in

795 the horizontal direction, and a larger concentration of deformation.

Looking at all the results indicates that, in case of isotropic stress state, the material plastic anisotropy is a predominant factor leading to the appearance of strain localisation in shear band mode around a gallery during its excavation. In fact, the excavation process does not lead to strain localisation unless a sufficient

800 material anisotropy is considered.

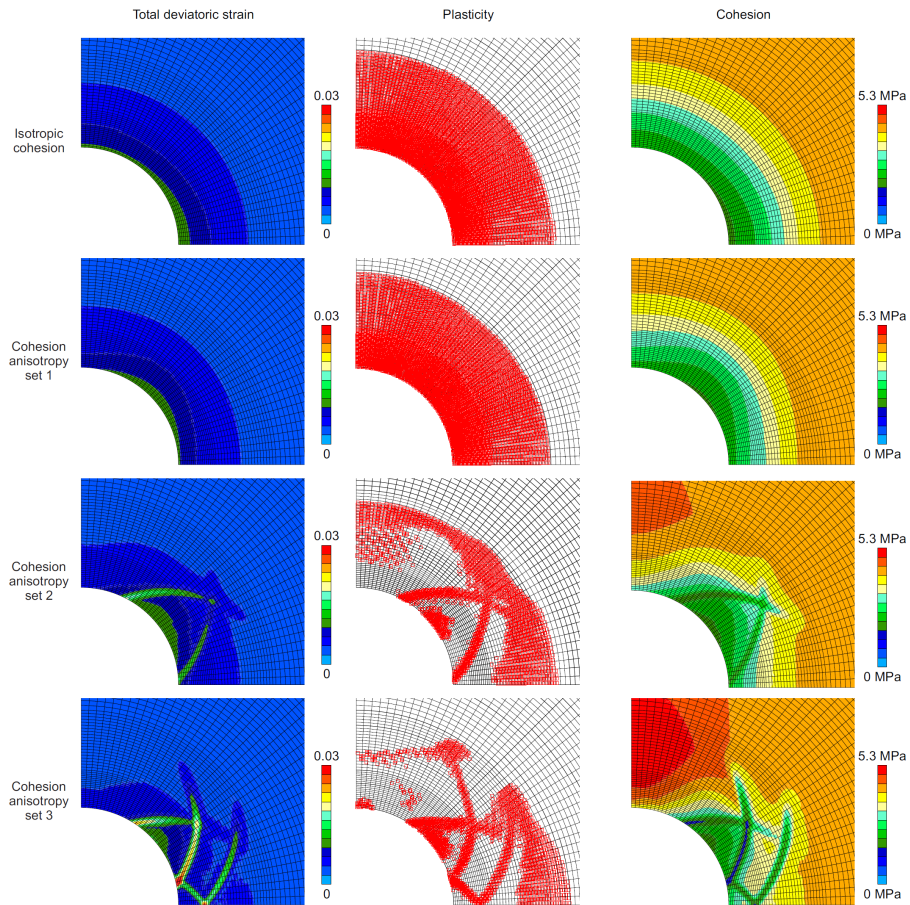


Figure 24: Shear strain localisation at the end of excavation for the different sets of anisotropic cohesion parameters.

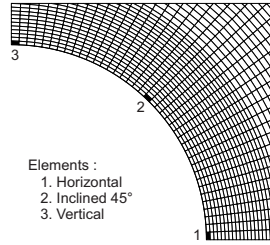


Figure 25: Elements on gallery wall chosen for the analysis of cohesion evolution during excavation.

The preferential development of shear bands in the inclined and horizontal directions can be explained by the evolution of the cohesion. To better illustrate this cohesion evolution, let us consider three elements on gallery wall illustrated in Fig. 25. For the anisotropic cohesion parameters of set 3, the evolution of cohesion, loading vector and yield index of those elements are detailed in Fig. 26. The cohesion evolution depends only on anisotropic effect when the element is in elastic state, and it depends on both anisotropic and softening effects when the element is in plastic state.

While the radial stress decreases and vanishes at gallery wall during the excavation, the orthoradial stress increases. This implies that the loading tends to be horizontal above and below the gallery which corresponds to a loading parallel to the horizontal isotropic planes. Then, the loading vector component l_3 decreases and the cohesion increases by evolving from its original value \bar{c} towards the left hand side of the cohesion curve in Fig. 23. It is in fact observed in Fig. 26 that l_3 decreases towards a value of zero above the gallery (vertical direction) which leads to an increase of the cohesion before plasticity is reached, then softening engenders the following cohesion decrease. On the contrary, the loading tends to be vertical or perpendicular to the horizontal isotropic planes on both left and right sides of the gallery, causing an increases of l_3 and an evolution of the cohesion from \bar{c} towards the right hand side of the cohesion curve. On this side of the curve, the cohesion decreases slightly before reaching its lowest value and may finally increase for an important increase of l_3 . This can be

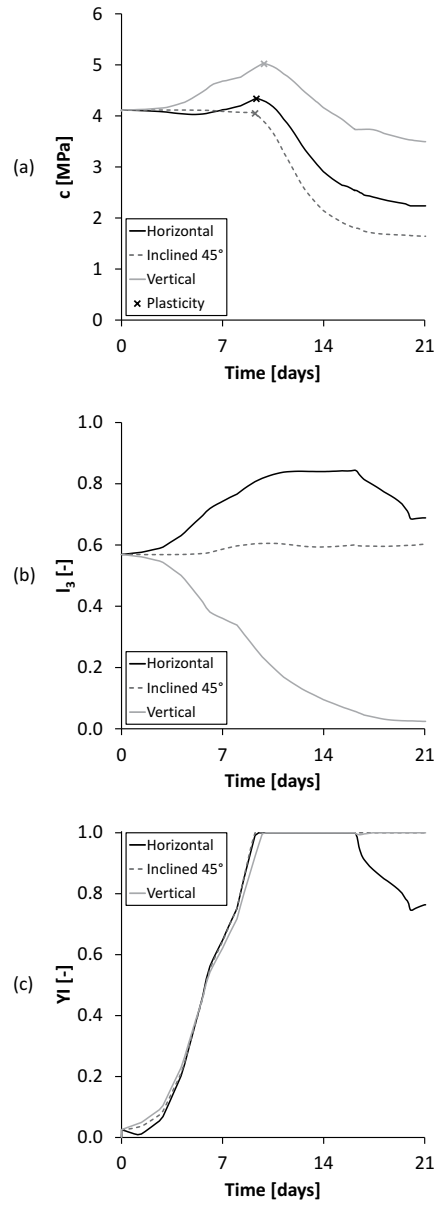


Figure 26: Cohesion (a), loading vector (b) and yield index (c) evolutions during the excavation for the set 3 of anisotropic cohesion parameters.

observed in Fig. 26 for the element located on the side of the gallery (horizontal direction). Nevertheless, the increase of l_3 is limited because the stress in the gallery axial direction does not cancel during the excavation (Eq. 45), thus the increase of cohesion before reaching plasticity and softening is lower than above the gallery. Concerning the element in the inclined direction (at 45° with the horizontal), l_3 remains almost constant, the cohesion remains low in the elastic regime and decreases rapidly due to softening.

This analysis of the cohesion indicates that the material is weaker in the inclined direction and the strain localisation is therefore initiated in that direction (Fig. 24). Furthermore, the material strengthening above and below the gallery leads to a preferential development of plasticity as well as strain localisation in the horizontal direction. The material plastic anisotropy is thus the cause of the excavation fractured zone shape and extension.

Let us now consider the development of the shear bands during the excavation for the anisotropic cohesion parameters of set 3. The evolution of the deviatoric strain increment, the total deviatoric strain, the plastic zone, the nodal velocity norm (with the global movements in the rock indicated with arrows) and the pore water pressure are illustrated in Fig. 27 for different instants during the excavation. One can observe that the strain localisation is initiated before $1 - \zeta = 0.08$ (15.4 days) with different shear bands that are in competition (see the deviatoric strain increment) but not fully developed (see the total deviatoric strain and the plastic zone). At this stage, the deformation slightly concentrates around the gallery in an inclined direction and we can observe that the velocity norms are greater for a direction lying between 25° and 45° with the horizontal direction. Furthermore, two shear bands fully develop before $1 - \zeta = 0.04$ (16.8 days) with elastic unloading in the outer material (the elastic unloading appears at $1 - \zeta = 0.057$ or 16.2 days in Fig. 26). The position and shape of those bands create a block of rock between them that tends to "unhook" from the gallery wall and to converge rapidly towards the gallery center (see the velocity and the global movements in Fig. 27). Finally, a supplementary shear band propagates with a reflection on the symmetry x-axis

before the end of the excavation $1 - \zeta = 0$ (21 days). It creates a second block
855 that converges rapidly towards the gallery center. These different stages of the
unloading with the initiation of strain localisation, the full development of some
shear bands and the varying shear band activity are similar to what has been
observed in the biaxial compression test results.

Fig. 27 also illustrates the pore water pressure evolution during the excava-
860 tion and the strain localisation process. A drainage progressively develops in
the gallery vicinity due to the imposed hydraulic boundary condition at gallery
wall. Negative pore pressures and pore pressures higher than the initial one are
observed as a result of hydro-mechanical coupling and shear bands activity. The
pore pressure variations in the rock remain low due to the low value of dilatancy
865 angle.

4.3.3. Gallery convergence

The shear band development inevitably influences the convergence of the
gallery. The convergence is defined by the variation of the gallery diameter
and is investigated in three directions : the horizontal, the vertical and the
870 inclined direction at 45° . It is illustrated in Fig. 28 for the anisotropic cohesion
parameters of set 3 both for localised and homogeneous solutions.

The homogeneous solution is obtained if the appearance of strain localisation
is avoided which can be done by increasing the second gradient elastic modulus
 D . This solution exhibits therefore a diffuse plastic zone and a quasi-isotropic
875 convergence. However, an anisotropic convergence is obtained for the localised
solution that reproduces the development of shear bands. This anisotropy can be
explained by relating the results of Fig. 27 and Fig. 28 (a) during the excavation
period. In fact, it is observed that the convergence at 45° increases more rapidly
than the other convergences from 12.5 days. This increase can be related to the
880 appearance of strain localisation and to the increase of nodal velocities towards
the gallery center in the inclined direction (visible at 15.4 days). Around 16.5
days, a slight fluctuation in the convergence curves is observed especially in
the 45° direction. It corresponds to the complete development of the shear

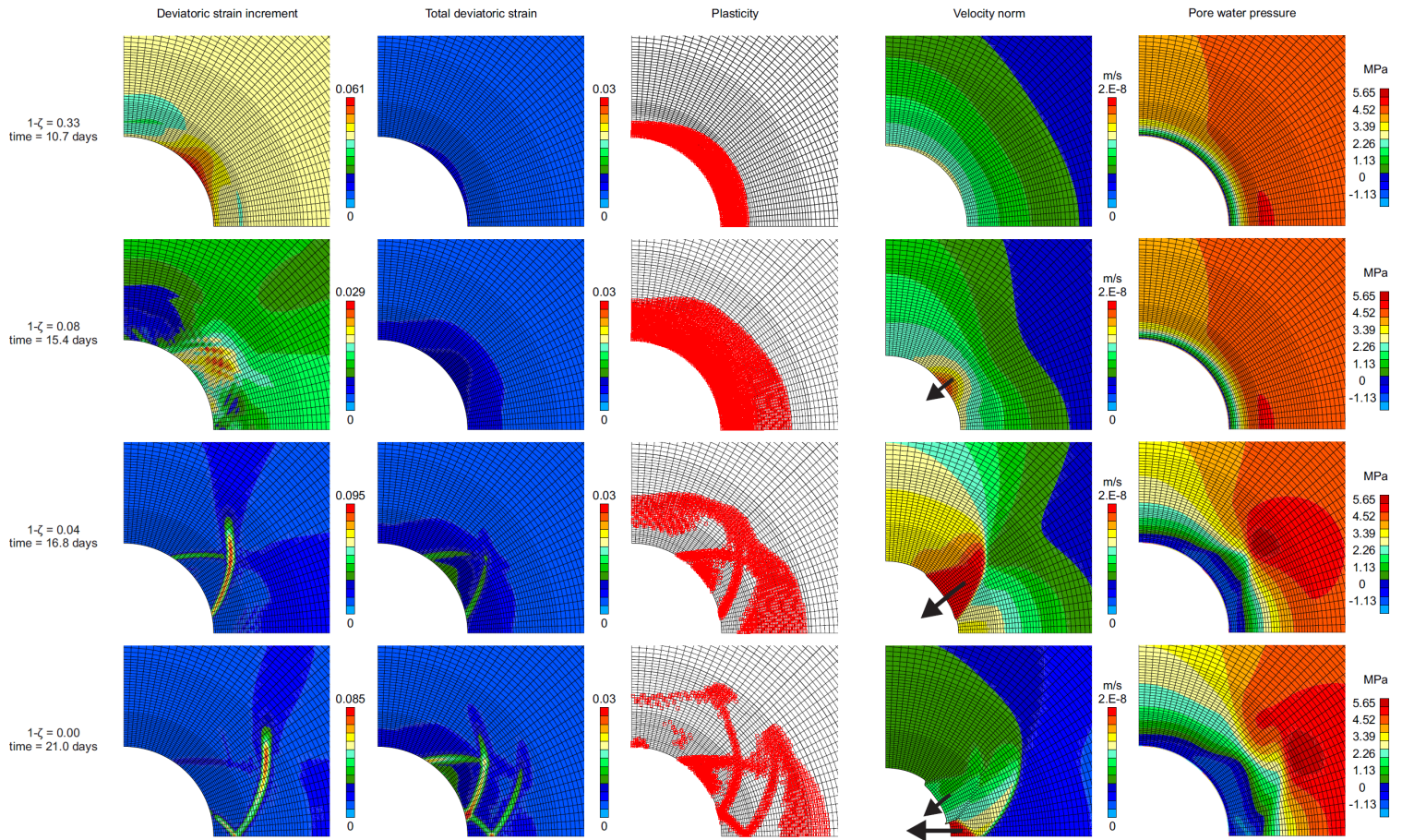


Figure 27: Development of shear strain localisation during the excavation for the set 3 of anisotropic cohesion parameters.

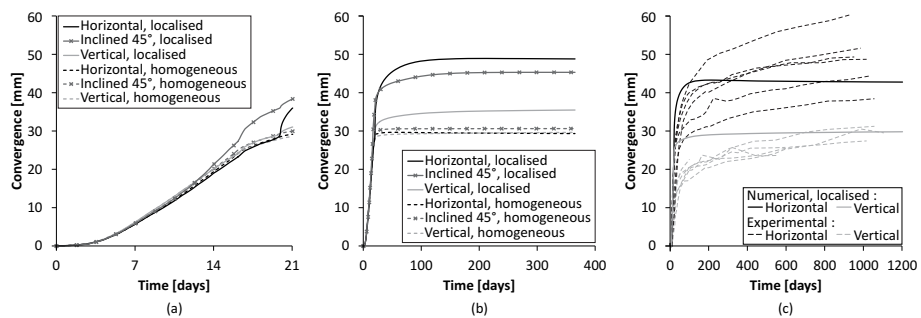


Figure 28: Gallery convergence during excavation (a), after excavation (b) and comparison to experimental measurements in the long term (c).

bands and to the movement towards the gallery center of the block located
885 between them (visible at 16.8 days). Around 20 days, we observe a strong
variation of the horizontal convergence which corresponds to the appearance of
the supplementary shear band and supplementary block that converges rapidly
(visible at 21 days).

At the end of excavation, the convergence at 45° is still greater than the two
890 other convergences but they can evolve afterwards because of hydro-mechanical
coupling and shear band activity that influence the different block movements.
The modelling has then been extended under constant zero radial stress and zero
pore water pressure at gallery wall. The resulting convergences (Fig. 28 (b)) are
greater than for the homogeneous case and highlight a strong anisotropy with
895 an important horizontal convergence. This indicates that the block at gallery
wall located in the horizontal direction continues to move significantly towards
the gallery center after the end of excavation, which is due to the progressive
drainage of the rock around the gallery and to hydro-mechanical coupling. Such
increase of convergence after the end of excavation was also observed by Pardoen
900 et al. (2015a).

The convergences can be compared with *in situ* experimental measurements
that are performed in the French underground research laboratory drilled in
Callovo-Oxfordian claystone (Armand et al., 2013; Guayacan-Carrillo et al.,
2015). A drift (GCS) oriented parallel to the major horizontal principal stress
905 and having a quasi-isotropic stress state of 12 MPa in its section is considered.
For the different convergence measurement sections (GCS-OHZ170B to G), the
experimental results indicate that the convergence is anisotropic and that it
increases in the long term (Fig. 28 (c)). The major convergence is measured
in the horizontal direction which corresponds to the location of the fractures
910 (Fig. 4 (top)).

The convergence measurement sections are installed inside the gallery just
after the excavation front which implies that the beginning of the measurements
corresponds to the seventh day of the numerical modelling. Thus, the numerical
convergences in Fig. 28 (c) are only detailed from that time, excluding the rock

915 mass deformation that develops before. One can observe that both horizontal
and vertical convergences are well reproduced, with a small overestimation of
the vertical one in the short term. For reproducing the convergence increase
in the long term the viscosity effect and creep deformations must be taken into
account.

920 5. Conclusions

The influence of cross-anisotropic properties on the development of shear
banding has been highlighted for geomechanical applications on rock. A cross-
anisotropic model including anisotropy of the elastic and plastic behaviours is
used together with an enriched model, the coupled local second gradient model,
925 that allows to correctly reproduce the shear strain localisation.

The shear banding appearance and development are well reproduced on small
rock specimens subjected to plane-strain biaxial compression. The material
strength (peak stress amplitude) as well as the shear banding pattern vary ac-
cording to the loading direction with respect to the microstructure (bedding
930 planes) orientation. The post-peak behaviour is also investigated and an evolu-
tion of the shear banding activity is observed.

On a large scale, the development of an excavation fractured zone composed
of shear bands around an underground gallery is also controlled by the material
anisotropy. In fact, the anisotropy of the plastic material behaviour is a pre-
935 vailing factor that governs the strain localisation onset and the banding pattern
(shape, location and orientation) in case of initial isotropic stress state. Differ-
ent amplitudes of anisotropy have been considered for the material cohesion and
strain localisation in shear bands appears around the gallery only if a sufficient
anisotropy amplitude is considered. This anisotropy is also the origin of the
940 anisotropic shape of the excavation fractured zone that displays a larger hori-
zontal extent. Furthermore, the numerical results also indicate that the shear
bands appearance and pattern are the cause of the convergence anisotropy.

Nonetheless, the change of the rock properties in the fractured zone still need

to be improved with a more accurate description of the the hydro-mechanical
 945 coupling. An evolution of the hydraulic permeability in the shear bands can be
 added in the model (Pardoen et al., 2014, 2015b) by considering a dependency
 with a mechanical parameter (Olivella & Alonso, 2008).

Acknowledgements

The authors are grateful for financial support from the FRIA-F.R.S.-FNRS,
 950 the National Funds of Scientific Research in Belgium.

List of symbols

General notations

\dot{a}	Time derivative of quantity a	s^{-1}
$a^{e/p}$	Elastic/plastic component of quantity a	—
$\sharp a$	Quantity a in orthotropic axes	—
$a_{\parallel/\perp}$	Quantity a in parallel/perpendicular di- rection related to the isotropic planes	—
$a_{0/f}$	Initial/final value of quantity a	—
a^t	Current configuration of quantity a at a given time t	—
a^*	Virtual quantity a	—
$a^{0/1}$	Quantity a outside/inside a shear band	—

Greek letters

α	Euler's rotation angle for isotropic planes orientation	$^\circ$
β	Lode angle	$^\circ$
Γ	Porous material boundary	m^2
Γ_σ	Part of Γ on which \bar{t}_i and \bar{T}_i are applied	m^2
Γ_q	Part of Γ on which \bar{q} is prescribed	m^2

δ_{ij}	Kronecker symbol	—
ϵ_{ij}	Total strain field	—
$\hat{\epsilon}_{ij}$	Deviatoric total strain field	—
$\hat{\epsilon}_{eq}$	Von Mises' equivalent deviatoric total strain (total deviatoric strain)	—
ϵ_z	Vertical strain for biaxial compression test	—
ζ	Stress deconfinement rate for gallery excavation	—
ζ_w	Pore water pressure deconfinement rate for gallery excavation	—
η	Yield surface convexity parameter	—
ϑ	Tangential coordinate	m
Θ	Shear band orientation	$^\circ$
$\Theta_{A/C/R}$	Arthur's, Coulomb's and Roscoe's angles for Θ	$^\circ$
κ	Deviatoric strain increment	—
λ_{ij}	Lagrange multipliers field	Pa
Λ	Plastic multiplier	—
μ_w	Water dynamic viscosity	$Pa\ s$
$\nu_{\parallel\perp/\parallel\parallel/\perp\parallel}$	Poisson's ratios	—
ξ	Cohesion softening ratio	—
ρ_s	Solid grains density	kg/m^3
ρ_w	Water density	kg/m^3
σ_{ij}	Cauchy total stress field	Pa
σ'_{ij}	Biot's effective stress field	Pa
$\tilde{\sigma}'_{ij}$	Jaumann effective stress rate	Pa/s
$\hat{\sigma}_{ij}$	Deviatoric total stress field	Pa
σ_i	Principal total stresses	Pa
σ'_i	Principal effective stresses	Pa

$\sigma_{H/h/v}$	Callovo-Oxfordian claystone <i>in situ</i> principal stresses	Pa
σ_c	Uniaxial compressive strength	Pa
σ_x	Confinement pressure for biaxial compression test	Pa
σ_z	Vertical total stress for biaxial compression test	Pa
$\sigma_{r,0}$	Initial pressure on gallery wall	Pa
σ_r^Γ	Fictive pressure on gallery wall	Pa
Σ_{ijk}	Double stress dual of h_{ijk}	$Pa\ m$
$\dot{\Sigma}_{ijk}$	Jaumann double stress rate	$Pa\ m/s$
τ_{ij}	Microstructure stress field (microstress)	Pa
v_{ij}	Microkinematic gradient field	—
φ	Friction angle	°
φ_{bif}	Friction angle at bifurcation	°
φ_c	Compression friction angle	°
φ_e	Extension friction angle	°
Φ	Porosity	—
ψ	Dilatancy angle	°
ψ_{bif}	Dilatancy angle at bifurcation	°
ψ_c	Compression dilatancy angle	°
ψ_e	Extension dilatancy angle	°
ω_{ij}	Spin rate tensor	s^{-1}
Ω	Porous material configuration (volume)	m^3

Roman letters

I_σ	First stress invariant	Pa
$II_{\hat{\sigma}}$	Second deviatoric stress invariant	Pa
$II_{\hat{\sigma}}^p$	Second deviatoric stress invariant at plastic state	Pa

$III_{\hat{\sigma}}$	Third deviatoric stress invariant	Pa
a_{ij}	Microstructure fabric tensor for cohesion	Pa
\hat{a}_{ij}	Deviatoric microstructure fabric tensor for cohesion	Pa
A_{ij}	Reduced deviatoric microstructure fabric tensor for cohesion	—
A_{\parallel}	Component of A_{ij} in the isotropic planes	—
\mathcal{A}_{ijkl}	Elastoplastic constitutive tangent tensor for large strain and rotations	Pa
A_{ijkl}^J	Jaumann's correction tensor for large strain and rotations	Pa
b_{ij}	Biot's tensor	—
$b_{\parallel/\perp}$	Biot's coefficients	—
b	Generalised Biot's coefficient	—
$b_{1/2}$	Cohesion evolution parameters	—
B_{φ}	Friction angle hardening coefficient	—
B_c	Cohesion softening coefficient	—
c	Cohesion	Pa
\bar{c}	Cohesion under isotropic loading	Pa
C_{ijkl}	Elastoplastic constitutive tangent tensor for small strain and rotations	Pa
$d_{1/2}$	Yield surface parameters	—
D	Second gradient elastic modulus	N
D_{ijkl}^e	Compliance elastic tensor	Pa^{-1}
dec_c	Cohesion softening shifting	—
dec_{φ}	Friction angle hardening shifting	—
Du_i	Normal derivative of u_i	—
e_i	Orthotropic coordinate axes	m

$E_{\parallel/\perp}$	Young's moduli	Pa
F	Yield surface	Pa
F_{ij}	Macrodeformation gradient field	—
g_i	Shear band velocity gradient field	s^{-1}
G	Plastic potential	Pa
$G_{\parallel\perp/\parallel\parallel/\perp\perp}$	Shear moduli	Pa
h_{ijk}	Microkinematic second gradient field	m^{-1}
k_{ij}	Intrinsic water permeability tensor	m^2
$k_{\parallel/\perp}$	Intrinsic water permeabilities	m^2
K	Generalised bulk modulus of the poroelastic material	Pa
K_s	Isotropic bulk modulus of the solid grains	Pa
l_i	Generalised loading vector	—
L_{ij}	Velocity gradient field	s^{-1}
m	Yield surface parameter	—
m_G	Plastic potential parameter	—
$m_{w,i}$	Water mass flow	$kg/m^2 s$
M_w	Water mass inside unit volume Ω	kg/m^3
n_i	Normal unit vector	—
p_w	Pore water pressure	Pa
p_w^Γ	Pore water pressure on gallery wall	Pa
q	Global deviatoric stress for biaxial compression test	Pa
\bar{q}	Input water mass per unit area	$kg/m^2 s$
$q_{w,i}$	Average speed of water relative to the solid grains	m/s
Q	Water sink term	$kg/m^3 s$
r	Gallery radius	m

r_c	Compression reduced radius of the yield surface	—
$r_{c,G}$	Compression reduced radius of the plastic potential	—
r_e	Extension reduced radius of the yield surface	—
$r_{e,G}$	Extension reduced radius of the plastic potential	—
R_{ij}	Rotation matrix	—
S_{ijkl}	Jaumann's correction tensor for large strain and rotations	—
t_i	Shear band interface traction force per unit area	Pa
\bar{t}_i	External traction force per unit area	Pa
\bar{T}_i	External double force per unit area	$Pa\ m$
u_i	Macroscale displacement field	m
u_r	Radial displacement	m
$\ v\ $	Velocity norm	m/s
$W_{1/2/3}$	Non-equilibrium forces of balance equations for iterative procedure	
x_i	Principal coordinate axes (x,y,z)	m
YI	Yield index	—

955 References

- Abelev, A. V., & Lade, P. V. (2003). Effects of cross anisotropy on three-dimensional behavior of sand. I: Stress-strain behavior and shear banding. *J Eng Mech*, 129, 160–166.
- Abelev, A. V., & Lade, P. V. (2004). Characterization of failure in cross-
960 anisotropic soils. *J Eng Mech*, 130, 599–606.

- Aifantis, E. C. (1984). On the microstructural origin of certain inelastic models. *J Eng Mater Technol*, 106, 326–330.
- Alshibli, K., Batiste, S., & Sture, S. (2003). Strain Localization in Sand: Plane Strain versus Triaxial Compression. *J Geotech Geoenviron Eng*, 129, 483–
965 494.
- Amadei, B. (1983). *Rock anisotropy and the theory of stress measurements* volume 2. New York: Springer-Verlag. Lecture Notes in Engineering Series.
- Anand, L. (1983). Plane deformations of ideal granular materials. *J Mech Phys Solids*, 31, 105–122.
- 970 Andra (2005a). *Dossier 2005 Argile. Synthesis: Evaluation of the Feasibility of a Geological Repository in an Argillaceous Formation, Meuse/Haute Marne Site*. Technical Report Paris, France.
- Andra (2005b). *Dossier 2005 Référentiel du site Meuse/Haute-Marne Tome 2 : Caractérisation comportementale du milieu géologique sous perturbation*.
975 Seconde édition Paris, France.
- Armand, G., Leveau, F., Nussbaum, C., de La Vaissiere, R., Noiret, A., Jaeggi, D., Landrein, P., & Righini, C. (2014). Geometry and properties of the excavation-induced fractures at the Meuse/Haute-Marne URL drifts. *Rock Mech Rock Eng*, 47, 21–41.
- 980 Armand, G., Noiret, A., Zghondi, J., & Seyedi, D. M. (2013). Short- and long-term behaviors of drifts in the Callovo-Oxfordian claystone at the Meuse/Haute-Marne Underground Research Laboratory. *J Rock Mech Geotech Eng*, 5, 221–230.
- Arthur, J. R. F., Chua, K. S., & Dunstan, T. (1977a). Induced anisotropy in a
985 sand. *Géotechnique*, 27, 13–30.
- Arthur, J. R. F., Dunstan, T., Al-Ani, Q. A. J. L., & Assadi, A. (1977b). Plastic deformation and failure in granular media. *Géotechnique*, 27, 53–74.

- Arthur, J. R. F., & Menzies, B. K. (1972). Inherent anisotropy in a sand. *Géotechnique*, *22*, 115–128.
- 990 Barnichon, J. D. (1998). *Finite Element Modelling in Structural and Petroleum Geology*. Ph.D. thesis Faculté des Sciences Appliquées, Université de Liège Belgium.
- Bazant, Z. P., Belytschko, T. B., & Chang, T. P. (1984). Continuum Theory for Strain Softening. *J Eng Mech*, *110*, 1666–1692.
- 995 Behlau, J., & Mingerzahn, G. (2001). Geological and tectonic investigations in the former Morsleben salt mine (Germany) as a basis for the safety assessment of a radioactive waste repository. *Eng Geol*, *61*, 83–97.
- Benallal, A., & Marigo, J. J. (2007). Bifurcation and stability issues in gradient theories with softening. *Modelling Simul Mater Sci Eng*, *15*, 283–295.
- 1000 Bernaud, D., & Rousset, G. (1992). La "nouvelle méthode implicite" pour l'étude du dimensionnement des tunnels. *Rev Franç Géotech*, *60*, 5–26.
- Biot, M. A. (1941). General theory for three-dimensional consolidation. *J Appl Phys*, *12*, 155–164.
- Blümling, P., Bernier, F., Lebon, P., & Martin, C. D. (2007). The excavation
1005 damaged zone in clay formations time-dependent behaviour and influence on performance assessment. *Phys Chem Earth*, *32*, 588–599.
- de Borst, R., & Mühlhaus, H. B. (1992). Gradient-dependent plasticity: Formulation and algorithm aspects. *Int J Numer Meth Engng*, *35*, 521–539.
- Bossart, P., Meier, P. M., Moeri, A., Trick, T., & Mayor, J. C. (2002). Geo-
1010 logical and hydraulic characterisation of the excavation disturbed zone in the Opalinus Clay of the Mont Terri Rock Laboratory. *Eng Geol*, *66*, 19–38.
- Bésuelle, P., Chambon, R., & Collin, F. (2006). Switching deformation modes in post-localization solutions with a quasibrittle material. *J Mech Mater Struct*, *1*, 1115–1134.

- 1015 Bésuelle, P., Desrues, J., & Raynaud, S. (2000). Experimental characterisation of the localisation phenomenon inside a vosges sandstone in a triaxial cell. *Int J Rock Mech Min Sci*, 37, 1223–1237.
- Carranza-Torres, C., & Fairhurst, C. (2000). Application of the Convergence-Confinement Method of tunnel design to rock masses that satisfy the Hoek-
1020 Brown failure criterion. *Tunn Undergr Sp Tech*, 15, 187–213.
- Casagrande, A., & Carillo, N. (1944). Shear failure of anisotropic materials. *J Boston Soc Civ Eng*, 31, 74–87.
- Chambon, R. (1986). Bifurcation and shear band localization an approach for incrementally non linear constitutive equations. *J Mec Theor Appl*, 5, 277–
1025 298.
- Chambon, R., & Caillerie, D. (1999). Existence and uniqueness theorems for boundary value problems involving incrementally non linear models. *Int J Solids Struct*, 36, 5089–5099.
- Chambon, R., Caillerie, D., & Hassan, N. E. (1998). One-dimensional localisa-
1030 tion studied with a second grade model. *Eur J Mech A-Solid*, 17, 637–656.
- Chambon, R., Caillerie, D., & Matsushima, T. (2001). Plastic continuum with microstructure, local second gradient theories for geomaterials : localization studies. *Int J Solids Struct*, 38, 8503–8527.
- Charlier, R. (1987). *Approche unifiée de quelques problèmes non linéaires de*
1035 *mécanique des milieux continus par la méthode des éléments finis (grandes déformations des métaux et des sols, contact unilatéral de solides, conduction thermique et écoulements en milieu poreux)*. Ph.D. thesis Faculté des Sciences Appliquées, Université de Liège Belgium.
- Charlier, R., Collin, F., Pardoën, B., Talandier, J., Radu, J. P., & Gerard, P.
1040 (2013). An unsaturated hydro-mechanical modelling of two in-situ experiments in Callovo-Oxfordian argillite. *Eng Geol*, 165, 46–63.

- Chen, L., Shao, J. F., & Huang, H. W. (2010). Coupled elastoplastic damage modeling of anisotropic rocks. *Comput Geotech*, 37, 187–194.
- Cheng, A. H. D. (1997). Material coefficients of anisotropic poroelasticity. *Int J Rock Mech Min Sci*, 34, 199–205.
- 1045 Collin, F. (2003). *Couplages thermo-hydro-mécaniques dans les sols et les roches tendres partiellement saturés*. Ph.D. thesis Faculté des Sciences Appliquées, Université de Liège Belgium.
- Collin, F., Caillerie, D., & Chambon, R. (2009a). Analytical solutions for the thick-walled cylinder problem modeled with an isotropic elastic second gradient constitutive equation. *Int J Solids Struct*, 46, 3927–3937.
- 1050 Collin, F., Chambon, R., & Charlier, R. (2006). A finite element method for poromechanical modelling of geotechnical problems using local second gradient models. *Int J Numer Meth Engng*, 65, 1749–1772.
- 1055 Collin, F., Levasseur, S., & Chambon, R. (2009b). Numerical post failure methods in multiphysical problems. *Eur J Environ Civ Eng*, 13, 983–1004.
- Collin, F., & Pardoën, B. (2013). Excavation damaged zone modelling in claystone with coupled second gradient model. In Q. Yang, J. M. Zhang, H. Zheng, & Y. Yao (Eds.), *Constitutive Modeling of Geomaterials* Springer Series in Geomechanics and Geoengineering (pp. 313–317). Springer Berlin Heidelberg.
- 1060 doi:10.1007/978-3-642-32814-5_42.
- Cosserat, E., & Cosserat, F. (1909). *Théorie des Corps Déformables*. Paris: Hermann.
- Coulomb, C. A. (1773). Essai sur une application des règles de maximis et minimis à quelques problèmes de statique, relatifs à l'architecture. *Académie Royale des Sciences*, 7, 343–382.
- 1065 Coussy, O. (2004). *Poromechanics*. Chichester: John Wiley & Sons.

- Delay, J., Vinsot, A., Krieguer, J. M., Rebours, H., & Armand, G. (2007).
 Making of the underground scientific experimental programme at the
 1070 Meuse/Haute-Marne underground research laboratory, North Eastern France.
Phys Chem Earth, 32, 2–18.
- Desrues, J. (1984). *La localisation de la déformation dans les matériaux gran-
 ulaires*. Ph.D. thesis Université Joseph Fourier, Institut National Polytech-
 nique Grenoble.
- 1075 Desrues, J. (1987). Manuel de Rhéologie des Géomatériaux. chapter Naissance
 des bandes de cisaillement dans les milieux granulaires : expérience et théorie.
 (pp. 279–298). Press ENPC.
- Desrues, J. (2005). Hydro-mechanical coupling and strain localization in satu-
 rated porous media. *Rev Eur Génie Civ*, 9, 619–634.
- 1080 Desrues, J., & Viggiani, G. (2004). Strain localization in sand: an overview of
 the experimental results obtained in Grenoble using stereophotogrammetry.
Int J Numer Anal Meth Geomech, 28, 279–321.
- Detournay, E., & Cheng, A. H. D. (1993). Comprehensive rock engineering:
 Principles, practice and projects. chapter 5 Fundamentals of Poroelasticity.
 1085 (pp. 113–171). Oxford: Pergamon Press volume 2 Analysis and Design
 Method.
- Diederichs, M. S. (2003). Rock Fracture and Collapse Under Low Confinement
 Conditions. *Rock Mech Rock Eng*, 36, 339–381.
- Duveau, G., Shao, J. F., & Henry, J. P. (1998). Assessment of some failure
 1090 criteria for strongly anisotropic materials. *Mech Cohes-Frict Mat*, 3, 1–26.
- Emsley, S., Olsson, O., Stenberg, L., Alheid, H. J., & Falls, S. (1997). *ZEDEX:
 A Study of Damage and Disturbance from Tunnel Excavation by Blasting and
 Tunnel Boring*. Svensk Kärnbränslehantering AB/Swedish Nuclear Fuel and
 Waste Management Co.

- 1095 Finno, R., Harris, W., Mooney, M., & Viggiani, G. (1996). Strain localization and undrained steady state of sands. *J Geotech Engrg*, *122*, 462–473.
- Finno, R., Harris, W., Mooney, M., & Viggiani, G. (1997). Shear bands in plane strain compression of loose sand. *Géotechnique*, *47*, 149–165.
- Gens, A., Garcia-Molina, A. J., Olivella, S., Alonso, E. E., & Huertas, F. (1998).
1100 Analysis of a full scale in situ test simulating repository conditions. *Int J Numer Anal Meth Geomech*, *22*, 515–548.
- Germain, P. (1973). The method of virtual power in continuum mechanics. Part 2 Microstructure. *SIAM J Appl Math*, *25*, 556–575.
- Graham, J., & Houlsby, G. T. (1983). Anisotropic elasticity of a natural clay.
1105 *Géotechnique*, *33*, 165–180.
- Guayacan-Carrillo, L. M., Sulem, J., Seyedi, D. M., Ghabezloo, S., Noiret, A., & Armand, G. (2015). Analysis of Long-Term Anisotropic Convergence in Drifts Excavated in Callovo-Oxfordian Claystone. *Rock Mech Rock Eng*, . doi:10.1007/s00603-015-0737-7.
- 1110 Guy, N., Seyedi, D. M., & Hild, F. (2012). A probabilistic nonlocal model for crack initiation and propagation in heterogeneous brittle materials. *Int J Numer Meth Engng*, *90*, 1053–1072.
- Han, C., & Drescher, A. (1993). Shear bands in biaxial tests on dry coarse sand. *Soils Found*, *33*, 118–132.
- 1115 Hill, R. (1958). A general theory of uniqueness and stability in elastic-plastic solids. *J Mech Phys Solids*, *6*, 236–249.
- Hill, R., & Hutchinson, J. W. (1975). Bifurcation phenomena in the plane tension test. *J Mech Phys Solids*, *23*, 239–264.
- Jaumann, G. (1911). Geschlossenes system physikalischer und chemischer differentialgesetze. (pp. 385–530). Sitzgsber. Akad. Wiss. Wien volume 120.
1120

- Jenq, Y. S., & Shah, S. P. (1988). Mixed-mode fracture of concrete. *Int J Fracture*, *38*, 123–142.
- Jirásek, M., & Rolshoven, S. (2009). Localization properties of strain-softening gradient plasticity models. part i: Strain-gradient theories. *Int J Solids Struct*, *46*, 2225–2238. 1125
- Kanatani, K. I. (1984). Distribution of directional data and fabric tensors. *Int J Eng Sci*, *22*, 149–164.
- Kotronis, P., Collin, F., Bésuelle, P., Chambon, R., & Mazars, J. (2007). Local Second Gradient Models and Damage Mechanics: 1D Post-Localization Studies in Concrete Specimens. In G. Exadaktylos, & I. Vardoulakis (Eds.), *Bifurcation, Instabilities and Degradation in Geomechanics* (pp. 127–142). Springer. 1130
- Lade, P. V. (2007). Modeling failure in cross-anisotropic frictional materials. *Int J Solids Struct*, *44*, 5146–5162.
- Lade, P. V., Nam, J., & Hong, W. P. (2008). Shear banding and cross-anisotropic behavior observed in laboratory sand tests with stress rotation. *Can Geotech J*, *45*, 74–84. 1135
- Lekhnitskii, S. G. (1963). *Theory of Elasticity of an Anisotropic Elastic Body*. San Francisco: Holden-Day.
- Lenoir, N., Bornert, M., Desrues, J., Bésuelle, P., & Viggiani, G. (2007). Volumetric digital image correlation applied to X-ray microtomography images from triaxial compression tests on argillaceous rock. *Strain*, *43*, 193–205. 1140
- Love, A. E. H. (1927). *A treatise on the mathematical theory of elasticity*. Cambridge University Press. (4th ed.).
- Marschall, P., Trick, T., Lanyon, G. W., Delay, J., & Shao, H. (2008). Hydro-mechanical evolution of damaged zones around a microtunnel in a claystone 1145

formation of the Swiss Jura mountains. San Francisco, California: American Rock Mechanics Association. The 42nd US Rock Mechanics Symposium (USRMS).

- 1150 Martin, C. D., & Lanyon, G. W. (2004). *Excavation Disturbed Zone (EDZ) in Clay Shale : Mont Terri*. Technical Report 2001-01 Mont Terri Project. With contributions from P Bossart and P Blümling.

Mehrabadi, M. M., & Cowin, S. C. (1980). Prefailure and post-failure soils plasticity models. *J Eng Mech Div, ASCE*, 106, 991–1003.

- 1155 Mindlin, R. D. (1964). Micro-structure in linear elasticity. *Arch Ration Mech An*, 16, 51–78.

Mindlin, R. D. (1965). Second gradient of strain and surface-tension in linear elasticity. *Int J Solids Struct*, 1, 417–438.

- Mokni, M., & Desrues, J. (1999). Strain localisation measurements in undrained plane-strain biaxial test on Hostun RF sand. *Mech Cohes-Frict Mat*, 4, 419–441.

Niandou, H., Shao, J. F., Henry, J. P., & Fourmaintraux, D. (1997). Laboratory investigation of the mechanical behaviour of tournemire shale. *Int J Rock Mech Min Sci*, 34, 3–16.

- 1165 Ochiai, H., & Lade, P. V. (1983). Three-dimensional behavior of sand with anisotropic fabric. *J Geotech Engrg*, 109, 1313–1328.

Oda, M., Nemat-Nasser, S., & Konishi, J. (1985). Stress-induced anisotropy in granular masses. *Soils Found*, 25, 85–97.

- Olivella, S., & Alonso, E. E. (2008). Gas flow through clay barriers. *Géotechnique*, 58, 157–176.

Panet, M., & Guellec, P. (1974). Contribution à l'étude du soutènement d'un tunnel à l'arrière du front de taille. In *Advances in rock mechanics, Proceedings*

of the 3rd International Congress on Rock Mechanics. Denver: International Society Rock Mechanics volume II.

- 1175 Panet, M., & Guenot, A. (1982). Analysis of convergence behind the face of a tunnel. In *Proceedings of the 3rd International Symposium : Tunnelling 82* (pp. 197–204). Brighton: Institution of Mining and Metallurgy.
- Papanastasiou, P. C., & Vardoulakis, I. G. (1992). Numerical treatment of progressive localization in relation to borehole stability. *Int J Numer Anal Meth Geomech*, *16*, 389–424.
- 1180
- Pardoen, B., Levasseur, S., & Collin, F. (2014). Excavation damaged zone modelling including hydraulic permeability evolution in unsaturated argillaceous rock. In N. Khalili, A. R. Russell, & A. Khoshghalb (Eds.), *Unsaturated Soils: Research and Applications* (pp. 1387–1393). London: CRC Press.
- 1185 doi:10.1201/b17034-203.
- Pardoen, B., Levasseur, S., & Collin, F. (2015a). Using local second gradient model and shear strain localisation to model the excavation damaged zone in unsaturated claystone. *Rock Mech Rock Eng*, *48*, 691–714. doi:10.1007/s00603-014-0580-2.
- 1190
- Pardoen, B., Levasseur, S., & Collin, F. (2015b). Using shear strain localisation to model the fracturing around gallery in unsaturated Callovo-Oxfordian claystone. In K. T. Chau, & J. Zhao (Eds.), *Bifurcation and Degradation of Geomaterials in the New Millennium* Springer Series in Geomechanics and Geo-engineering (pp. 285–291). Springer. doi:10.1007/978-3-319-13506-9_41.
- 1195
- Peerlings, R. H. J., de Borst, R., Brekelmans, W. A. M., & de Vree, J. H. P. (1996a). Gradient enhanced damage for quasi-brittle materials. *Int J Numer Meth Engng*, *39*, 3391–3403.
- Peerlings, R. H. J., de Borst, R., Brekelmans, W. A. M., de Vree, J. H. P., & Spee, I. (1996b). Some observations on localisation in non-local and gradient damage models. *Eur J Mech A/Solids*, *15*, 937–953.
- 1200

- Pietruszczak, S. (2010). Fundamentals of plasticity in geomechanics. chapter 7, Description of inherent anisotropy in geomaterials. (pp. 133–156). Leiden, The Netherlands: CRC Press/Balkema.
- 1205 Pietruszczak, S., Lydzba, D., & Shao, J. F. (2002). Modelling of inherent anisotropy in sedimentary rocks. *Int J Solids Struct*, *39*, 637–648.
- Pietruszczak, S., & Mroz, Z. (2000). Formulation of anisotropic failure criteria incorporating a microstructure tensor. *Comput Geotech*, *26*, 105–112.
- Pietruszczak, S., & Mroz, Z. (2001). On failure criteria for anisotropic cohesive-frictional materials. *Int J Numer Anal Meth Geomech*, *25*, 509–524.
- 1210 Pietruszczak, S. T., & Mróz, Z. (1981). Finite element analysis of deformation of strain-softening materials. *Int J Numer Meth Engng*, *17*, 327–334.
- Pijaudier-Cabot, G., & Bazant, Z. P. (1987). Nonlocal damage theory. *J Eng Mech*, *113*, 1512–1533.
- Rice, J. R. (1976). The localization of plastic deformation. In W. T. Koiter (Ed.), 1215 *Theoretical and Applied Mechanics* (pp. 207–220). North-Holland Publishing Company volume 1.
- Rice, J. R., & Rudnicki, J. W. (1980). A note on some features of the theory of localization of deformation. *Int J Solids Struct*, *16*, 597–605.
- Roscoe, K. H. (1970). The influence of strains in soils mechanics. *Géotechnique*, 1220 *20*, 129–170. Tenth Rankine lecture.
- Rudnicki, J. W., & Rice, J. R. (1975). Conditions for the localisation of deformation in pressure sensitive dilatant materials. *J Mech Phys Solids*, *23*, 371–394.
- 1225 Salehnia, F., Collin, F., Li, X. L., Dizier, A., Sillen, X., & Charlier, R. (2015). Coupled modeling of Excavation Damaged Zone in Boom clay: Strain localization in rock and distribution of contact pressure on the gallery’s lining. *Comput Geotech*, *69*, 396–410. doi:10.1016/j.compgeo.2015.06.003.

- Shuttle, D. A., & Smith, I. M. (1988). Numerical simulation of shear band formation in soils. *Int J Numer Anal Meth Geomech*, *12*, 611–626.
- 1230 Simo, J. C., Oliver, J., & Armero, F. (1993). An analysis of strong discontinuities induced by strain-softening in rate-independent inelastic solids. *Comput Mech*, *12*, 277–296.
- Tejchman, J., Bauer, E., & Wu, W. (2007). Effect of fabric anisotropy on shear localization in sand during plane strain compression. *Acta Mech*, *189*, 23–51.
- 1235 Thakur, V. (2007). *Strain localization in sensitive soft clays*. Ph.D. thesis Norwegian University of Science and Technology Trondheim.
- Toupin, R. (1962). Elastic materials with couple-stresses. *Arch Ration Mech An*, *11*, 385–414.
- Triantafyllidis, N. (1980). Bifurcation phenomena in pure bending. *J Mech Phys Solids*, *28*, 221–245.
- 1240 Tsang, C. F., & Bernier, F. (2004). Definitions of excavation disturbed zone and excavation damaged zone, in Impact of the excavation disturbed or damaged zone (EDZ) on the performance of radioactive waste geological repositories. In *Proceedings European Commission CLUSTER Conference and Workshop on EDZ in Radioactive Waste Geological Repositories*. Luxembourg.
- 1245 Tsang, C. F., Bernier, F., & Davies, C. (2005). Geohydromechanical processes in the Excavation Damaged Zone in crystalline rock, rock salt, and indurated and plastic clays - in the context of radioactive waste disposal. *Int J Rock Mech Min Sci*, *42*, 109–125.
- 1250 Valès, F., Minh, D. N., Gharbi, H., & Rejeb, A. (2004). Experimental study of the influence of the degree of saturation on physical and mechanical properties in tournemire shale (france). *Appl Clay Sci*, *26*, 197–207.
- VanEekelen, H. A. M. (1980). Isotropic yield surfaces in three dimensions for use in soil mechanics. *Int J Numer Anal Meth Geomech*, *4*, 98–101.

- 1255 Vardoulakis, I. (1979). Bifurcation analysis of the triaxial test on sand samples. *Acta Mech*, 32, 35–54.
- Vardoulakis, I. (1980). Shear band inclination and shear modulus of sand in biaxial tests. *Int J Numer Anal Meth Geomech*, 4, 103–119.
- Vardoulakis, I. (1981). Bifurcation analysis of the plane rectilinear deformation
1260 on dry sand samples. *Int J Solids Struct*, 17, 1085–1101.
- Vardoulakis, I., Goldscheider, M., & Gudehus, Q. (1978). Formation of shear bands in sand bodies as a bifurcation problem. *Int J Numer Anal Meth Geomech*, 2, 99–128.
- Viggiani, G., & Desrues, J. (2004). Geotechnical Innovations. chapter Experimental
1265 observation of shear banding in stiff clay. (pp. 649–658). Essen: Verlag Glückauf.
- Wang, X. (1993). *Modélisation numérique des problèmes avec localisation de la déformation en bandes de cisaillement*. Ph.D. thesis Université de Liège Liège.
- 1270 Wileveau, Y., & Bernier, F. (2008). Similarities in the hydromechanical response of Callovo-Oxfordian clay and Boom Clay during gallery excavation. *Phys Chem Earth*, 33, S343–S349.
- Wu, S., & Wang, X. (2010). Mesh Dependence and Nonlocal Regularization of One-Dimensional Strain Softening Plasticity. *J Eng Mech*, 136, 1354–1365.
- 1275 Yang, D., Chanchole, S., Valli, P., & Chen, L. (2013). Study of the anisotropic properties of argillite under moisture and mechanical loads. *Rock Mech Rock Eng*, 46, 247–257.
- Zervos, A., Papanastasiou, P., & Vardoulakis, I. (2001a). Modelling of localisation and scale effect in thick-walled cylinders with gradient elastoplasticity.
1280 *Int J Solids Struct*, 38, 5081–5095.

Zervos, A., Papanastasiou, P., & Vardoulakis, I. (2001b). A finite element displacement formulation for gradient elastoplasticity. *Int J Numer Meth Engng*, 50, 1369–1388.